DOCTORAL THESIS

Measurement of the Zodiacal Light Absolute Intensity through Fraunhofer Line Spectroscopy

Department of Physics, Graduate School of Science and Technology, Kwansei Gakuin University

Author
Masaki Hanzawa

Supervisor
Prof. Shuji Matsuura

January 23, 2024

Acknowledgments

First of all, I would like to express my great appreciation to Professor Shuji Matsuura for giving me the opportunity to analyze astronomical spectra since I was a fourth-year undergraduate student. I am proud to have been able to pursue my research to the doctoral level under him.

In completing this thesis, I would first like to express my great appreciation to Ranga-Ram Chary of the California Institute of Technology for conducting this observation. I also thank Aoi Takahashi of the Astrobiology Center for the opportunity to analyze this data. I also thank Dr.Sano, Dr.Takimoto, and Mr.Tome for their cooperation in various aspects of data analysis.

Furthermore, the days I spent with the nearly 60 members of Matsuura Laboratory are the most precious memories for me. I would like to express my gratitude to all of you and wish you all better days.

Finally, I would like to express my great appreciation to my parents and younger siblings for their active support for the path I wish to pursue.

This thesis is reviewed by Prof. Masaaki Kusunose, Prof. Junko Hiraga, and Prof. Shuji Matsuura.

ABSTRACT

Measuring the absolute brightness of the zodiacal light (ZL), which is the sunlight scattered by interplanetary dust particles, is important not only for understanding the physical properties of the dust but also for constraining the extragalactic background light (EBL) by subtracting the ZL foreground. We describe the results of high-resolution spectroscopic observations of the night sky in the wavelength range from 300 nm to 900 nm with the Double spectrograph on the Hale telescope to determine the absolute brightness of the ZL continuum spectra from the Fraunhofer absorption line intensities. The observed fields are part of the fields observed by the Spitzer Space Telescope for the EBL study. Assuming that the spectral shape of the zodiacal light is identical to the solar spectrum in a narrow region around the Fraunhofer lines, we decomposed the observed sky brightness into multiple emission components by the amplitude parameter fitting with spectral templates of the airglow, ZL, diffuse Galactic light, integrated starlight, and other isotropic components including EBL. As a result, the ZL component with the Ca II $\lambda\lambda$ 393.3, 396.8 nm Fraunhofer lines around 400 nm is clearly separated from the others in all fields with uncertainties around 20%, mainly due to the template errors and the time variability of the airglow. Observed ZL brightness in most of the observed fields is consistent with the modeled ZL brightness calculated by combining the most conventional ZL model at 1250 nm based on the Diffuse Infrared Background Experiment and the observational ZL template spectrum based on the Hubble Space Telescope. However, the ecliptic plane observation is considerably fainter than the ZL model, and this discrepancy is discussed in terms of the optical properties of the interplanetary dust accreted in the ecliptic plane.

Contents

List of Figures

List of Tables

Chapter 1

Introduction

1.1 Zodiacal Light

Zodiacal light (ZL) is the scattered sunlight by interplanetary dust (IPD) particles. To understand the physical parameters of the IPD particles, the observation of the ZL brightness is important. The ZL brightness at optical wavelength can ignore the thermal emission (Kelsall et al., 1998) and this brightness along the line of sight ($I_{\rm ZL}$) is expressed as

$$I_{\rm ZL} = \int F_{\odot}(R) n(x, y, z) A \Phi(\theta) dl, \tag{1.1}$$

where $F_{\odot}(r)$ is the solar flux at the location of the particle, r is the distance of an IPD particle relative to the Sun, $n(x, y, z)$ is the number density at position (x, y, z), A is the albedo of the IPD particles, $\Phi(\theta)$ is the phase function for the scattering angle θ, and l is the distance along the line-of-sight from the observer. There is also an ecliptic latitude dependence on $n(x, y, z)$, resulting in the ZL being brightest in the ecliptic plane. Figure 1.1 shows the geometry of ZL observation.

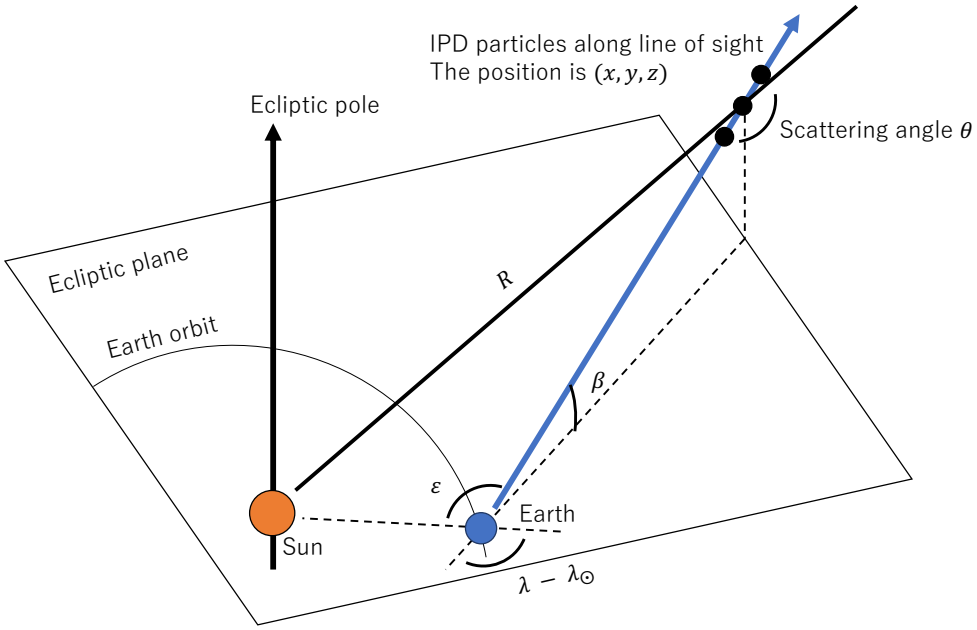

Figure 1.1: The geometry of ZL brightness on the Earth. The observed field is ecliptic latitude β and heliocentric-ecliptic longitude $(\lambda - \lambda_\odot)$, where λ means the ecliptic longitude of observed field and $\lambda_\odot$ means the ecliptic longitude of the Sun. R in the figure means the distance from the Sun to IPD particles through line-of-sight, ε means the solar elongation and θ means the scattering angle of the sunlight by IPD particles. The blue arrow means the line of sight of the observer.

IPD particles are removed from the solar system by the Poynting-Robertson effect and radiation pressure from sunlight. Therefore, IPD must be continuously supplied to maintain the ZL brightness, and the spatial distribution of IPD depends on the source of the particles. As shown in figure 1.2, there are three main types of sources of IPD particles. The first is the Jupiter Familly Comets, which are most abundant near the ecliptic plane and almost none near the ecliptic pole (Liou et al., 1995; Nesvorný et al. , 2010). The second is the asteroid-origin comet, which is present only at certain ecliptic latitudes (Nesvorný et al. , 2003; Sykes et al., 1986). The third is the Oort Cloud comet, which is caused by dust from the Oort Cloud and is isotropically distributed (Poppe , 2016). By combining these models of the dust distribution for each source of IPD particles with the observed ZL brightness, we can estimate the three-dimensional spatial distribution of IPD particles.

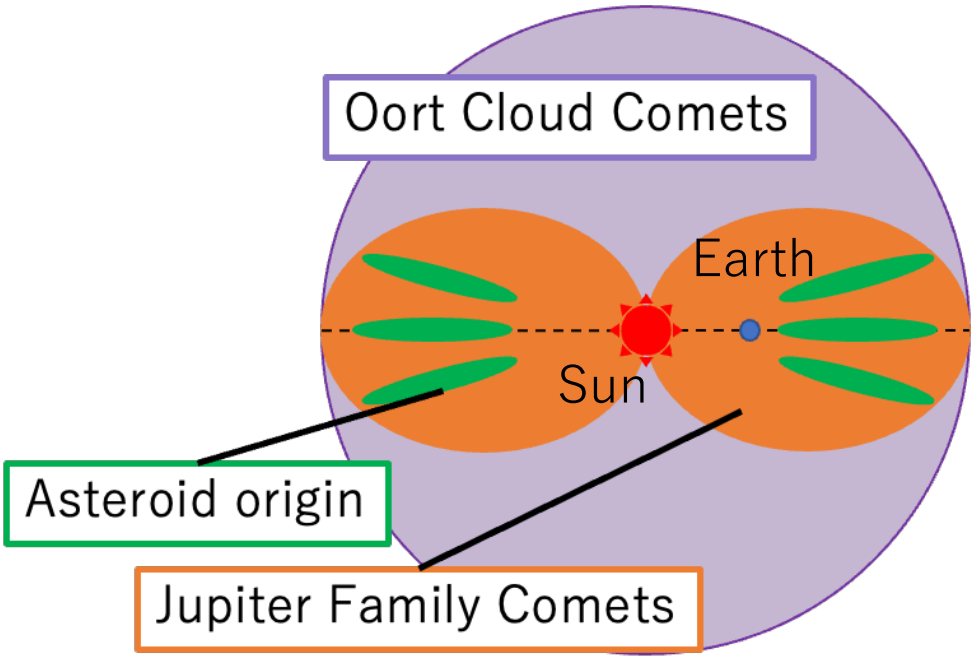

Figure 1.2: Schematic image of distribution of IPD particles.

Estimating the brightness of the ZL is important not only for studying IPD but also for the measurement of the extragalactic background light (EBL), which is the integral of all photon intensities emitted and absorbed from the birth of the universe to the present. The EBL measurement could potentially constrain the model of primitive galaxies and black holes that were born during the re-ionization of the universe. The EBL measurement in the visible and near-infrared have been made by the Cosmic Infrared Background Experiment (CIBER; Matsuura et al., 2017), the Hubble Space Telescope (HST; Carleton et al., 2022; Kawara et al., 2017), New Horizons (Lauer et al. , 2022; Symons et al. , 2023), the Diffuse Infrared Background Experiment on board the Cosmic Background Explorer (COBE/DIRBE, e.g., Dwek and Arendt, 1998), the Infrared Telescope in the Space (IRTS; Matsumoto et al., 2015) and AKARI (Tsumura et al., 2013). Because models and measurements of EBL have discrepancies (e.g. Kashlinsky et al. , 2018), high accuracy of measurement of EBL is important. As shown in figure 1.3, the brightness of the EBL is about 10 % of the ZL. Therefore, measuring ZL with high precision helps to reduce the uncertainty of the EBL.

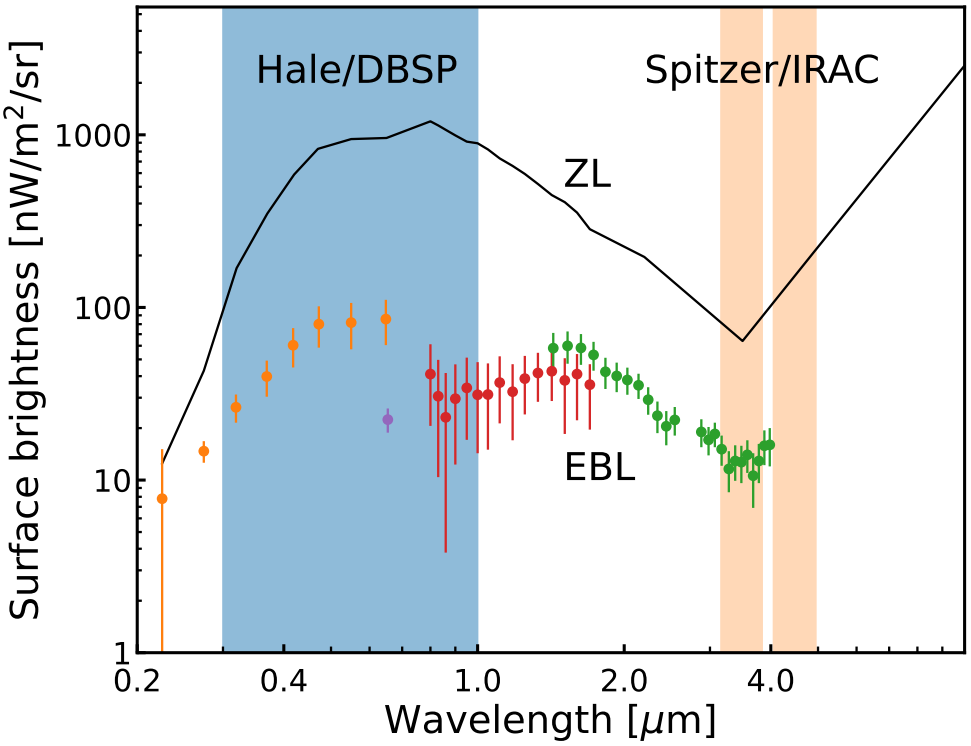

Figure 1.3: Compilation of EBL and ZL intensity from UV to NIR. The black line shows the ZL spectrum in the ecliptic plane (Kawara et al., 2017; Kelsall et al., 1998; Matsuura et al., 2017). The color plots show the previous EBL measurement, the orange plots are HST (Kawara et al., 2017), the red plots are CIBER (Matsuura et al., 2017), the purple plot is New Horizons (Symons et al. , 2023), and the greens are IRTS (Matsumoto et al., 2015). The color regions are the range of our observations, the blue is night-sky observation with the Hale telescope, and the oranges are the EBL measurement with the *Spitzer* Space Telescope, which is the collaborative observation with Hale.

Our current best models of ZL brightness are constrained by DIRBE and Far-Infrared Absolute Spectrometer (FIRAS) observations on board the COBE. This model assumed three different spatial distributions of IPD particles, smooth cloud, dust bands, and circumsolar ring. However, current studies have suggested other isotropically distributed IPD particles besides these components (c.f. Sano et al., 2020). Therefore,various models fit to the data have an uncertainty of more than 10% in fields with high ecliptic latitude (Kelsall et al., 1998; Wright, 1998). In Appendix D, we describe the

details of the Kelsall model which is the current best model of ZL brightness.

The uncertainty of the best model of ZL brightness greatly affects the uncertainty of EBL measurements. Thus, we measured the ZL brightness through night-sky observation. Since this method does not depend on the ZL model, we can obtain the ZL brightness which does not include the uncertainty of the model.

1.2 Night-Sky Observation

The night-sky brightness observed in the ground-based telescope consists of five major components: atmospheric airglow (hereafter airglow), ZL, diffuse Galactic light (DGL), integrated starlight (ISL), and EBL, shown as figure 1.4. For the broad-band photometry of the night-sky brightness in many previous studies, the separation of ZL from the other components contributing to the night-sky brightness has been done by modeling the ZL distribution depending on the ecliptic coordinates. However, the isotropic or quasi-isotropic component of ZL (c.f. Sano et al., 2020) cannot be decomposed by such a method. One of the promising methods to separate the entire ZL with no model uncertainty is to observe Fraunhofer lines in the ZL spectrum, as was done in Bernstein et al. (2002) and Brian (2007). The ZL brightness is measured from the absorption depth of the Fraunhofer line assuming the line-to-continuum ratio for the ZL spectrum is the same as that of the sun in a narrow range around the spectral line with no effect of the broad spectral feature of IPD. The Fraunhofer lines contribution from the ISL and DGL are estimated from the stellar population distribution in the Galaxy. The spectrum of the EBL of distant galaxies is assumed to be smooth because of the superimpose of galaxies with various redshifts (Driver et al. , 2016).

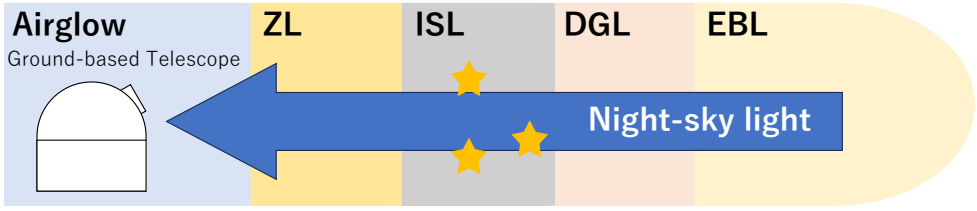

Figure 1.4: Components of the night-sky brightness. The night-sky brightness is composed of five major components for ground-based observation.

In addition, the airglow has no Fraunhofer lines. Therefore, the airglow spectrum does not affect the absorption intensity of the Fraunhofer lines in the night-sky spectrum.

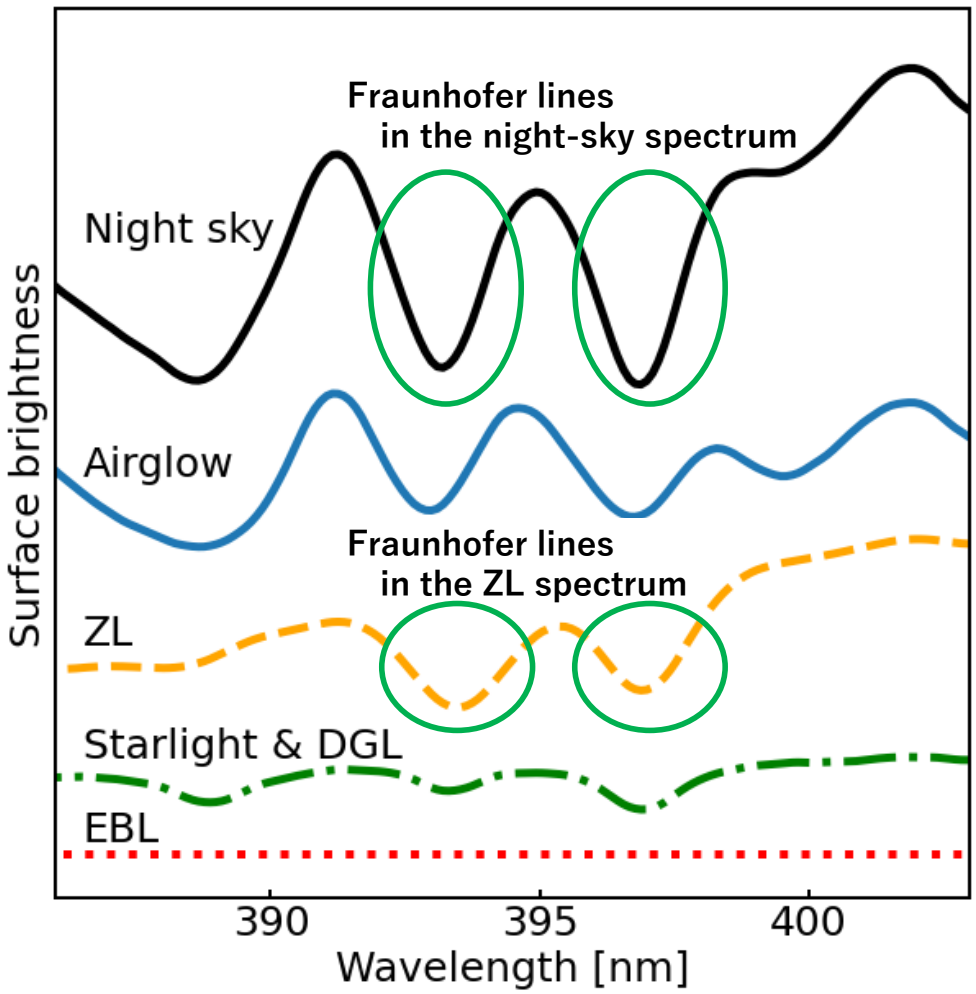

Figure 1.5: Comparing the spectral shape of the night-sky component. The spectral shape of the airglow is an example of this observation. The spectral shape of the ZL is modeled by the solar spectrum (MODTRAN; Berk et al., 2014, 2015). Since the spectral shapes of starlight and DGL are almost identical, they are shown together in the same spectrum (Mattila et al., 2017). The shape of EBL is assumed to be a constant value. We can estimate the ZL brightness to compare the Fraunhofer lines in the night sky and the ZL spectrum.

1.3 Spitzer Space Telescope

The Fraunhofer line measurement of ZL was conducted in collaboration with the EBL measurement by the *Spitzer* Space Telescope. *Spitzer*, which had the Earth-trailing orbit and was located ~ 1.7 AU from the Earth at the time of the observation as shown in figure 1.6, was one of the few spacecraft that could observe along a line of sight through the zodiacal cloud which did not go through the Earth. It therefore allowed measurements of the zodiacal dust which were not affected by potential local particle overdensities.

The days before the end of the *Spitzer* mission was the only time that the project approved the use of the IRAC shutter which would enable a measurement of the dark current and bias on the arrays. A dedicated program was undertaken which allowed the measurement of the diffuse sky brightness at 3600 nm and 4500 nm using the imaging capabilities of IRAC. The observations were executed in the final week of the warm *Spitzer* observing campaign, number 274 in week 948. The observations consisted of 122 Astronomical Observing Requests (AORs), spanning a range of ecliptic latitude and longitude, within the *Spitzer* pointing constraints on those days (the red arrows in figure 1.6).

However, the 3600 nm band has contributions from both the scattered and thermal components of the zodiacal dust while the 4500 nm band is dominated by the thermal component. By targeting the same fields in the optical from a ground-based telescope at a time when the Earth is at the location where *Spitzer* was when it executed the observations, one could potentially obtain an independent measurement of the scattering component which can then be separated from the 3600 nm measurements.

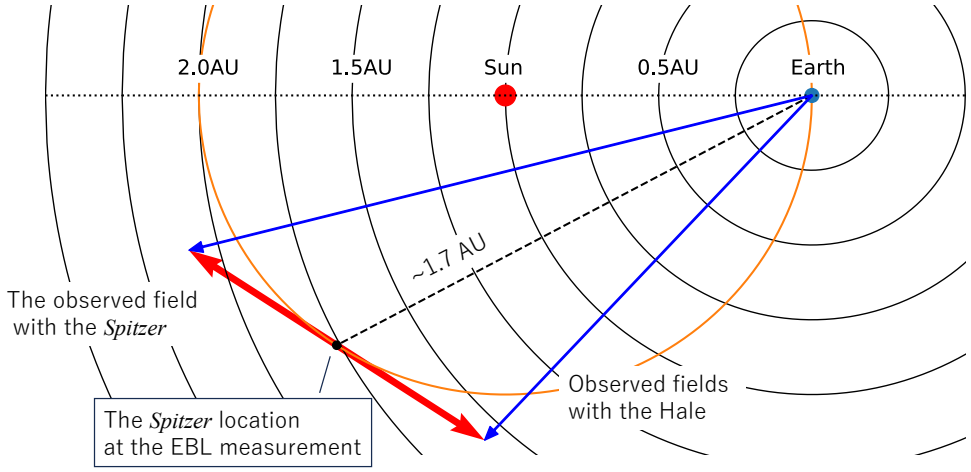

Figure 1.6: The region of observing field with the *Spitzer*. The blue arrows show the observed field of Fraunhofer measurement with the Hale Telescope.

1.4 Outline of this thesis

This thesis is organized into 6 chapters. In chapter 2, we describe our spectral observations of the night sky with the Hale telescope. In chapter 3, we describe the primary analysis we performed to generate the spectra of the night sky. The observed images are two-dimensional imaging data reflecting the number of photons produced by the brightness of the night sky. Therefore, we need to generate the spectrum of surface brightness from this image data. In chapter 4, we describe the brightness of the ZL as measured by this observation. The night-sky spectrum is composed of airglow, DGL, starlight, and EBL other than the ZL. Therefore, we show in this chapter the method by which we have separated them. In chapter 5 we discuss our results. A summary of this thesis is given in chapter 6.

Chapter 2

Observation

2.1 Instrument

We conducted spectroscopic observations of the night sky with the Hale telescope at the Palomar Observatory. The Hale telescope is a visible light telescope located on Palomar Mountain in California, USA, with an aperture of 5 meters (200 inches). Figure 2.1 shows the dome of the Hale telescope. The Hale telescope is equipped with a double spectrograph (DBSP; Oke & Gunn , 1982), which splits the light from celestial objects into short wavelength (blue channel; 340 nm $< \lambda <$ 550 nm) and long wavelength (red channel; 500 nm $< \lambda <$ 1000 nm) components for simultaneous observations. Figure 2.2 shows the optical system of DBSP. Table 2.1 shows the DBSP setup used for this observation.

Table 2.1: DBSP specifications and settings for this observation

	Blue channel	Red channel
Detectors	CCD	LBNL
Array size	460 × 2835	440 × 4141
Slit length	128”	128”
Slit width	1”	1”
Scale	0.389 arcsec/pixel	0.293 arcsec/pixel
Grating	600/4000 lines/mm	316/7500 lines/mm
Wavelength range	300 - 550nm	550 - 900nm
Wavelength dispersion	0.11 nm / pixel	0.15 nm / pixel
Wavelength resolution of FWHM	0.33 nm/pixel	0.44 nm/pixel

Figure 2.1: Nighttime long exposure of the Hale Telescope dome. Image credit is the Palomar Observatory [1].

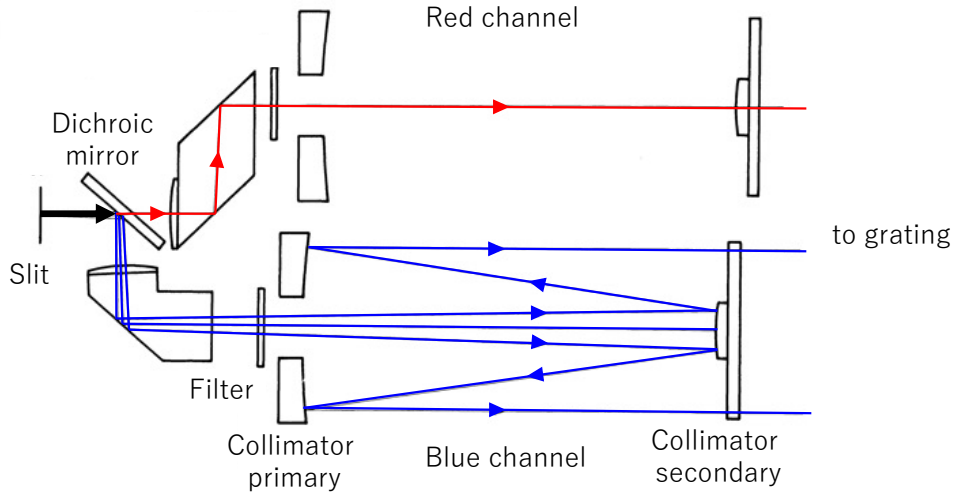

Figure 2.2: The optics of DBSP from Figure1 in Oke & Gunn (1982).

[1] https://sites.astro.caltech.edu/palomar/about/telescopes/hale.html

2.2 The night-sky observation

Our spectroscopic observations of the night sky were conducted on 2020 September 15-16. The individual fields were targeted because they were also the targets of closed-shutter observations with the IRAC instrument of the *Spitzer* Space Telescope towards the end of the mission in 2020 January (Fazio et al., 2004).

Since *Spitzer* is in the Earth trailing orbit with pointing constraints that are roughly 90 degrees away from the sun, the time of these Palomar observations was coordinated to trace roughly the same path through the zodiacal cloud to get a handle on the dust column density. Figure 2.3 shows the observed field plotted against the ZL intensity map by the Kelsall model based on COBE/DIRBE data (Kelsall et al., 1998).

The choice of slits differed between the night sky and standard star observations. For the night sky, a slit with 1" × 128" field-of-view was used, while for standard star observations, a slit with 10" × 128" field-of-view was employed. We obtained 4, 6, and 5 exposures for WISE-J0301, NEP-1-1, and other fields, respectively, where we integrated photons for 300 seconds per exposure. The standard stars of our observation are WD 1817+788 (hereafter WD 1817) and SDSS J072752 (hereafter SDSS J0727), which are the white dwarf stars used in Calamida et al. (2019). We obtained 5 exposures for 1" × 128" and 6 exposures for 10" × 128" of WD 1817. Additionally, we obtained 5 exposures for 1" × 128" and 3 exposures for 10" × 128" of SDSS J0727. The standard stars were observed before and after the night-sky observations. We summarized the information of our observations in table 2.2.

Table 2.2: Observation Fields

Field	Target[1]	Time (Local) [2] UT - 7 hr	$Ra_{J2000.0}$ deg	$Dec_{J2000.0}$ deg	Elon.[3] deg	Elat.[3] deg	Solar elongation deg	Airmass	Exptime [4] sec
Bias		9/15 16:43 - 16:47	-	-	-	-	-	-	0
Darks		16:53 - 17:06	-	-	-	-	-	-	60
Arc ATLAS	CL	17:10 - 17:15	-	-	-	-	-	-	30
Dome Flats		18:50 - 19:44	-	-	-	-	-	-	60
WD 1817+788	Std	23:16 - 23:28	273.6	78.9	86.8	77.6	-	1.63	60
WD 1817+788[5]	Std	23:29 - 23:36	273.6	78.9	86.8	77.6	-	1.62	60
NEP-1-1	NS	23:41 - 9/16 00:13	269.9	66.2	262.2	89.7	90.0	1.65	300
Elon295Step26	NS	00:19 - 00:46	294.0	-4.9	295.0	16.5	120.0	2.47	300
WISE-J0301	NS	00:57 - 1:18	46.7	1.1	44.6	-15.7	127.3	1.71	300
Elon66Step17	NS	1:22 - 1:49	64.1	21.3	66.0	0.0	107.7	1.61	300
Elon66Step28	NS	1:58 - 2:25	60.8	37.7	66.3	16.7	106.7	1.24	300
Elon66Step29	NS	2:29 - 2:56	60.4	38.0	65.9	17.0	107.0	1.16	300
Elon66Step30	NS	3:00 - 3:27	60.3	38.5	66.0	17.5	106.9	1.09	300
Elon82Step6	NS	3:32 - 3:59	82.8	6.3	82.5	-17.0	91.2	1.50	300
Elon82Step7	NS	4:03 - 4:30	82.8	5.8	82.5	-17.5	91.2	1.37	300
SDSS J072752	Std	4:34 - 5:01	112.0	32.2	108.8	10.2	-	1.48	300
SDSS J072752[5]	Std	5:01 - 5:17	112.0	32.2	108.8	10.2	-	1.36	300
Darks		5:20 - 6:08	-	-	-	-	-	-	300

[1] "CL" means wavelength calibration lamp, "Std" means standard star, and "NS" means night sky.
[2] The time at Palomar Observatory. The year of this observation is 2020.
[3] "Elon." and "Elat." mean the ecliptic longitude and latitude.
[4] "Exptime" means the exposure time of each observation in units of seconds.
[5] Using 10" slit width. Other is using 1" slit width.

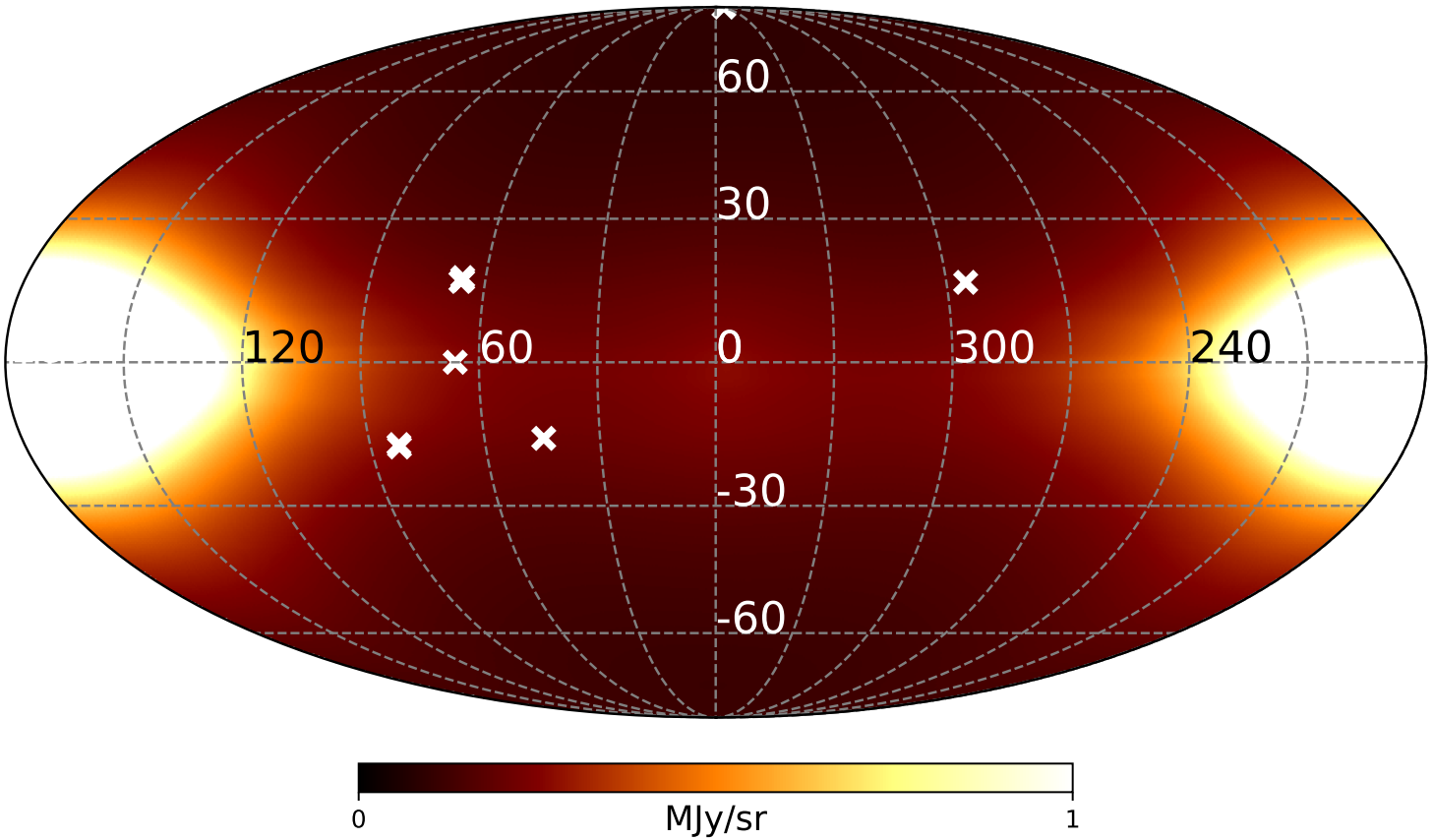

Figure 2.3: The observed fields of the night sky plotted on the ZL all-sky map. All-sky map of the ZL is a Mollweide projection in geocentric ecliptic coordinates. The background image represents the ZL brightness at 1250 nm calculated using *Zodipy* (San et al., 2022). The blue plots indicate the fields of our observation (see "Elon." and "Elat." in table 2.2).

Chapter 3

Data reductions

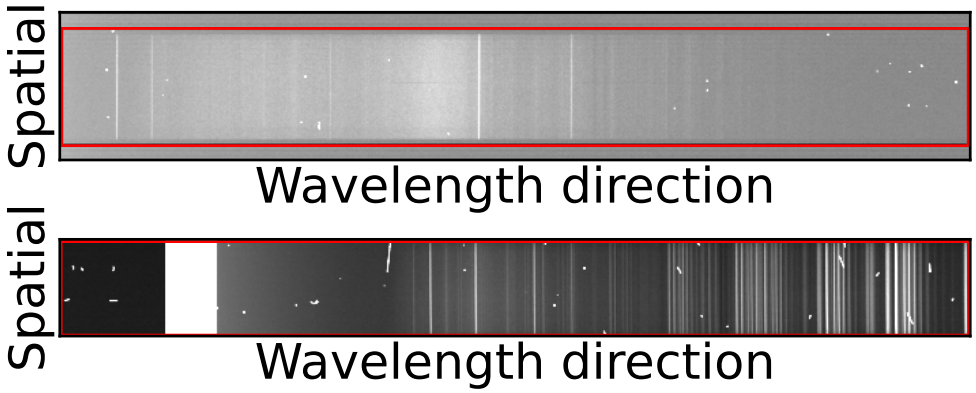

Figure 3.1: Observed raw images of the blue channel (top) and red channel (bottom). The region enclosed by red lines represents the "observed region", while the area outside it is the masked region, referred to as the "overscan region". The horizontal direction corresponds to the wavelength direction, covering a wavelength range from 300 nm to 550 nm at the blue channel and from 500 nm to 10000 nm at the red channel. 1 pixel of wavelength direction is the same as 0.11 nm at the blue channel and 0.15 nm at red channel. The vertical direction represents the spatial direction, with a slit width of 128".

The raw data observed by the Hale telescope is a two-dimensional image as shown in figure 3.1. This data is divided into two regions: the "observation region" (indicated by the red region in figure 3.1), which detects the signal from the emission from the source, and the "overscan" region, which detects instrument-derived signals such as bias currents and dark currents outside

of the observation region. The vertical direction (spatial in figure 3.1) corresponds to the length of the slit, and the horizontal direction (wavelength direction in figure 3.1) shows the wavelength dispersion.

Since the observed data cannot be handled as is, we created a spectrum showing the surface brightness at each wavelength through the procedure shown in figure 3.2. This section describes this procedure in detail.

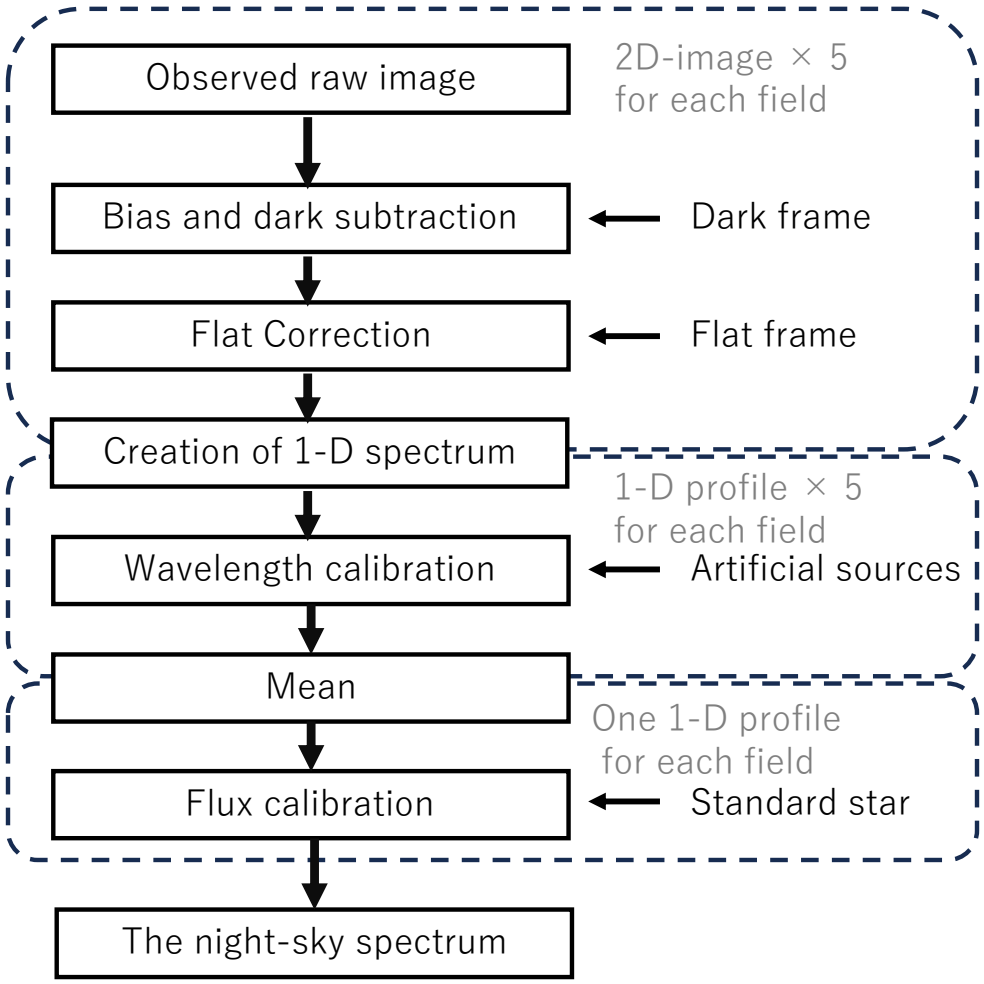

Figure 3.2: Outline of data reduction.

3.1 Subtraction of bias and dark frame

The observed raw images contain signals from the night sky and signals from bias current and dark current. Therefore, we performed three steps to remove the signals from bias and dark current. First, the dark frames obtained with each exposure time were averaged and we defined them as "superdark". This was done to reduce the noise of the dark frame itself. Next, we subtracted the super dark frame from the observations with the same exposure time. Finally, to subtract the bias, we subtracted the average value of the "overscan region" in the dark-subtracted data from each pixel count in the observed region. The uncertainty caused by this step is calculated by propagating the standard error, which is the standard deviation divided by the number of samples, of superdark frame and overscan region in dark-subtracted data and this value is 0.001% of dark-subtracted data.

3.2 Flat fielding

The sensitivity of a detector varies depending on the position of the pixel receiving the signal, and it is necessary to correct this in the observed data. Therefore, we corrected the sensitivity variation through the following three steps, using the observation data of a uniform light beam called a frat frame. First, we normalized the data by their median value in each wavelength direction in each flat frame. Second, we created an average flat frame, defined as "superflat", by averaging the flat frames with the same exposure time. Finally, we divided the data with dark removal by the superflat. Figure 3.3 shows the observed data before and after flat correction. The indeterminacy caused by this procedure was calculated by propagating the standard error of the flat frame and the indeterminacy of the section 3.1, which was 0.01% for the flat-corrected data.

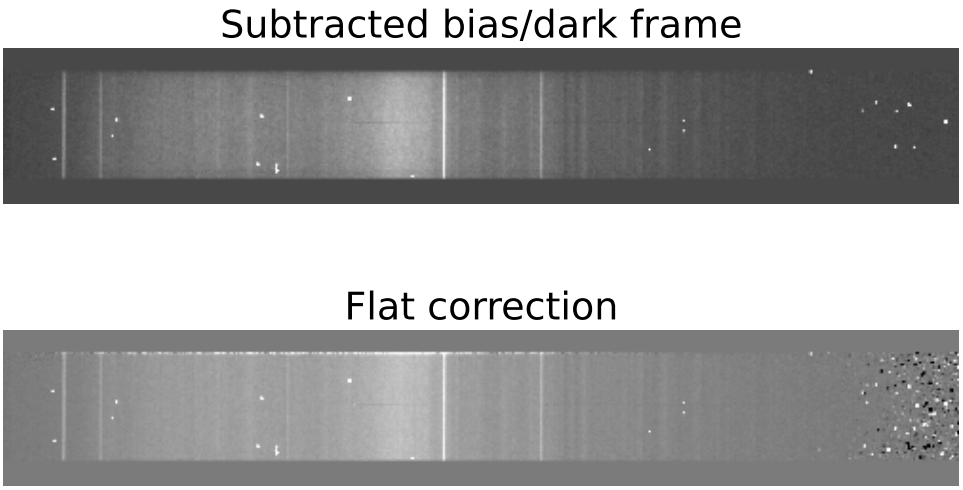

Figure 3.3: Before and after flat correction at blue frame. The top shows before flat correction (dark-subtracted data) and the bottom shows after.

3.3 Creation of one dimensional spectrum

The night-sky spectra extend over the field of view along the spatial direction of the slit. We therefore generated spectra from the observed images using the following procedure. First, since the Elon66Step17 and WISE-J0301 data contained a celestial source, we assumed a Gaussian distribution for its spatial extent and masked the region within 5 times the standard deviation of Gaussian. Next, we made spectra of observed signals per wavelength pixel for each pixel row along the wavelength direction. Third, we averaged the spectra of each spatial position at the same wavelength after wavelength calibration. Finally, we averaged the spectra at the same field. The uncertainty due to this step was computed by propagating the standard error for the average signal in the spatial direction and the uncertainty in sections 3.1 and 3.2. The value is 1.5% of the observed data.

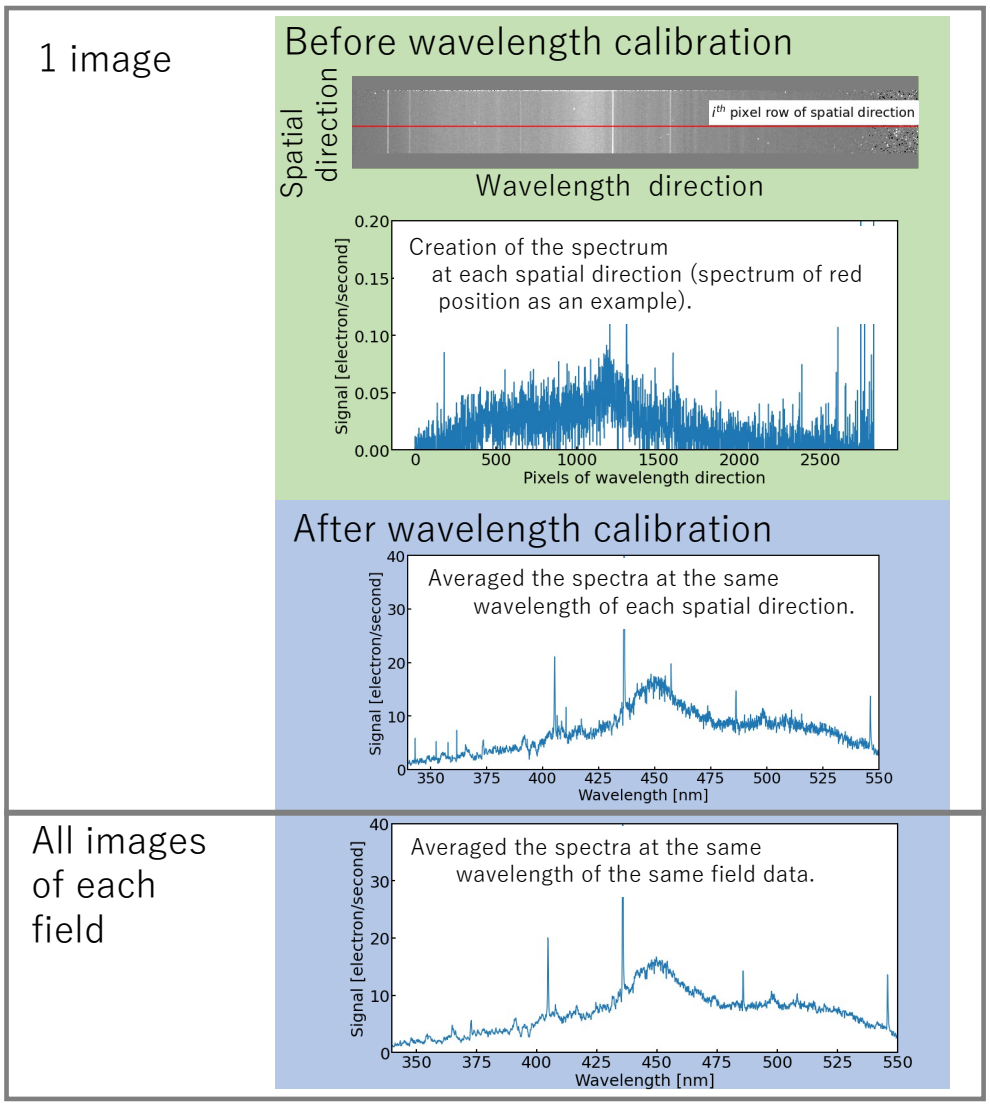

Figure 3.4: The outline of creation of one-dimensional spectrum. The example data is Elon82Step6.

3.4 Wavelength calibration

To perform the wavelength calibration, we observed artificial sources consisting of Fe and Ar emission lines in the blue channel and He, Ne, and Ar in the red channel. The line widths of the emission lines are 0.14 nm (1 Gaussian sigma). To match wavelength pixels to wavelength, we identified 16 strong emission lines in the artificial sources. We calculated the conversion factor from wavelength pixel to wavelength with a linear function for each pixel row of each spatial direction. In figure 3.5, we show an example of the conversion factor of wavelength calibration. The R^2 values inserted in the figure are the coefficient of determination defined as the equation 3.1.

$$R^2 = 1 - \frac{\sum_i (y_i - f_i)^2}{\sum_j (y_j - \bar{y})^2} \tag{3.1}$$

where y_i and y_j mean the i^{th} and j^{th} values of the plotted data, $\bar{y}$ means the average value of y, and f_i means the estimated i^{th} value with linear fitting. For standard stars, the conversion factor was calculated based on the same region as the slit position where the standard star is observed. On the other hand, since the night-sky light is detected over the entire slit, a conversion factor was calculated for each spatial pixel.

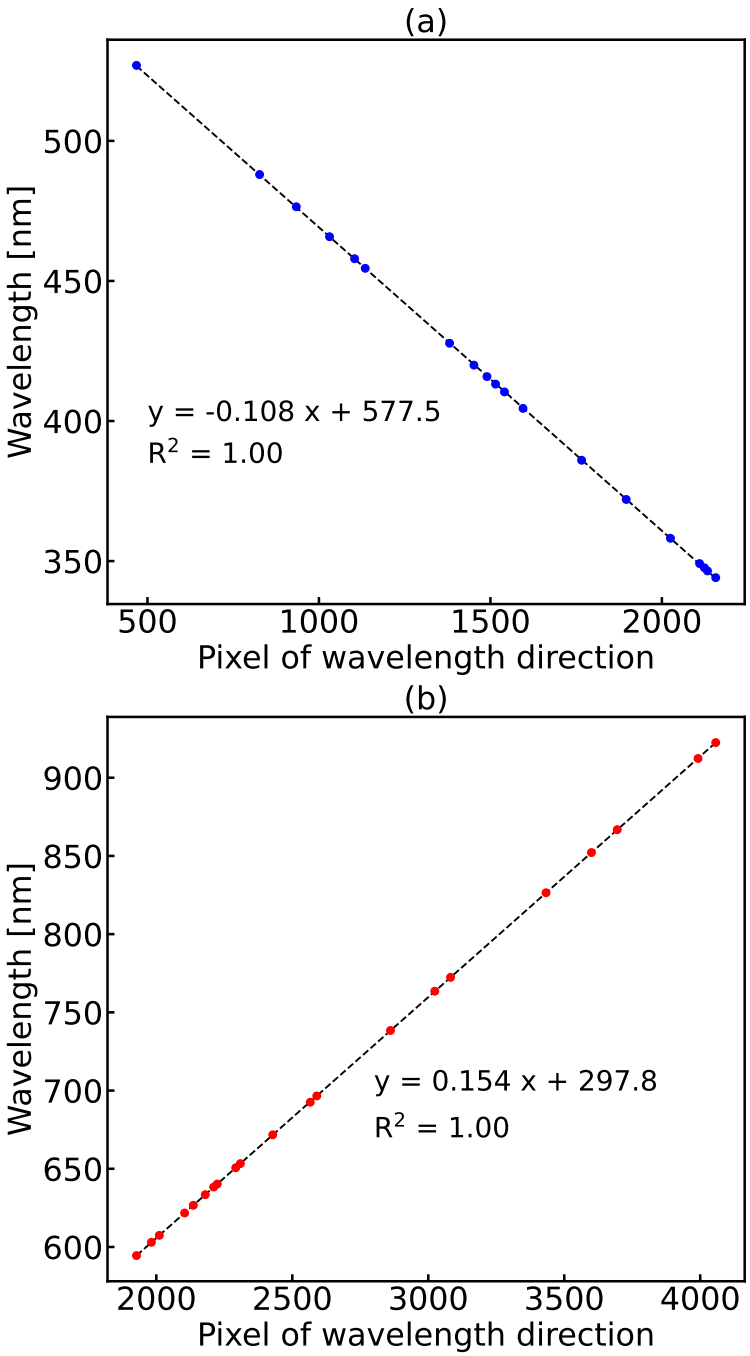

Figure 3.5: The conversion factor of wavelength calibration. Figure (a) shows the blue channel and (b) shows the red channel. The linear function in each figure is an equation that converts pixels in the wavelength direction to wavelength. R^2 is the coefficient of determination defined as equation 3.1.

3.5 Flux calibration

The observed spectra that created these steps are expressed in units of electron s^{-1}, which must be converted to the physical unitsnW m^{-2} sr^{-1}. To perform this, we generated the spectrum of SDSS J0727, which was observed with that slit width is 10". We assumed that the point-spread function (PSF) of the stellar source follows a Gaussian distribution when the flat fielding was already applied to the observed images. We summed up the signals within a range of ± 5 times the standard deviation in the spatial direction from the center of the standard star to calculate the signal from the standard star at each wavelength pixel. To select the signal from the standard star, we subtracted the background signal from the summed-up signals of the standard star. The background signals were obtained by averaging the outside of the standard star at each wavelength pixel and multiplying the pixel count of the range of the standard star. We show observed and modeled spectra of SDSS J0727 in figure 3.6 [The modeled spectrum is by Narayan et al. (2019)]. With the spectrum obtained through this method, we calculated the flux calibration factor $C(\lambda)$, using the equation 3.2.

$$C(\lambda) = \frac{F(\lambda)}{S(\lambda)\Omega 10^{0.4\chi\tau(\lambda)}}, \tag{3.2}$$

where $F(\lambda)$ is the modeled flux (Narayan et al., 2019) of standard stars in units of nW m^{-2} nm^{-1}, $S(\lambda)$ is the total signal within the PSF of the observed standard star in units of electron s^{-1}, Ω is the solid angle in units of sr pix^{-1}, χ is the airmass value along the line of sight at this observation, and $\tau(\lambda)$ is the atmospheric extinction curve in units of magnitude $airmass^{-1}$ shown in figure 3.7 (a). We were unable to calculate the atmospheric extinction curve for this observation due to thin clouds. Therefore, we used the Hayes & Latham (1975) as the atmospheric extinction curve for the Palomar Observatory. The standard star used to create the flux calibration factor is SDSS J0727 (see appendix A), and the slit width is 10", which can detect more than 99% of the light of the standard star as shown figure 3.7 (b). Therefore, no additional correction is required for slit loss. In figure 3.8, we show flux calibration factors of red and blue channels. We converted photocurrent units electron s^{-1} to nW m^{-2} sr^{-1} by multiplying the observed night-sky spectra by $C(\lambda)$. We show an example of the observed night-sky spectrum in figure 3.9.

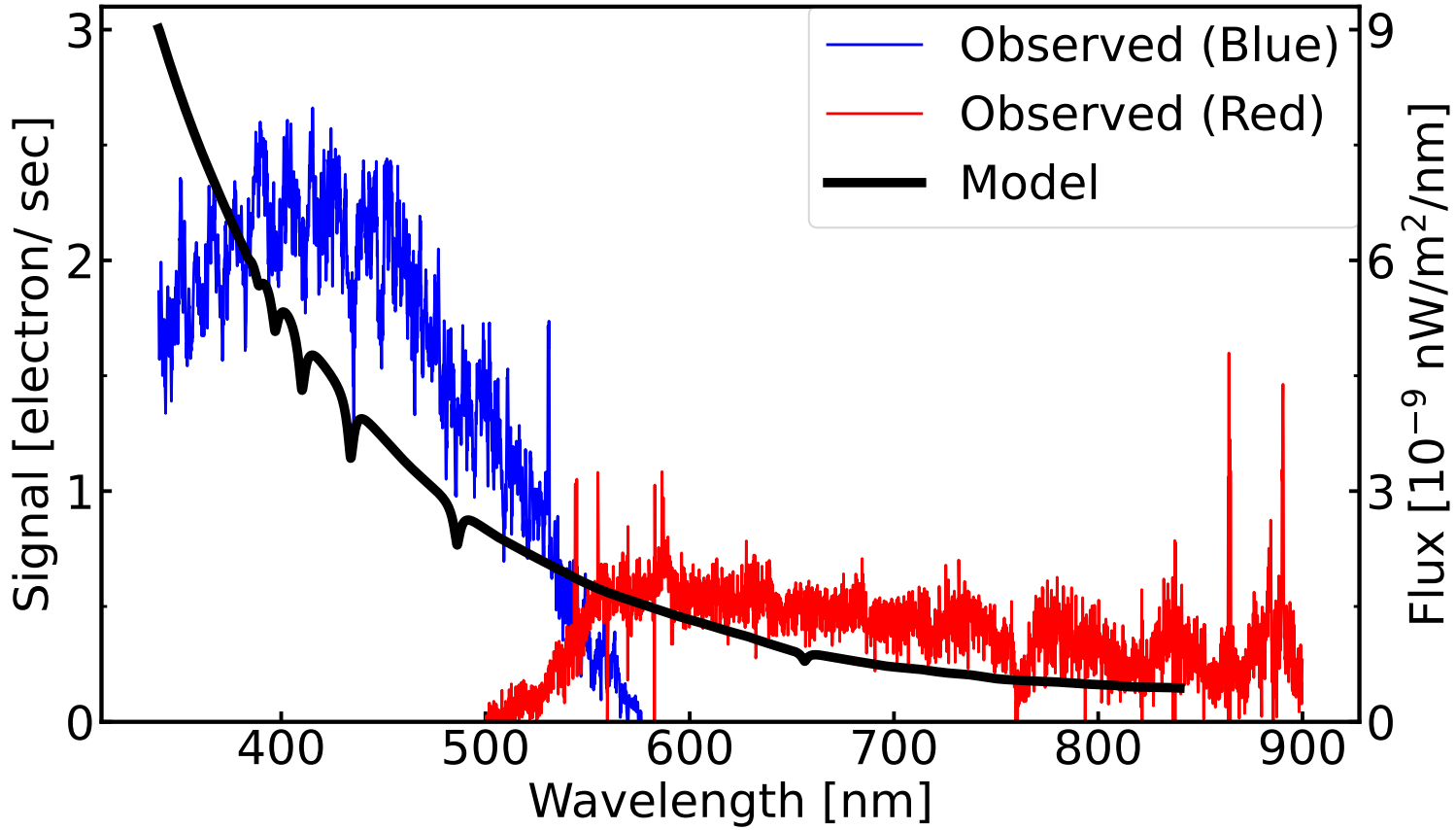

Figure 3.6: Observed and modeled spectra of the standard star (SDSS J0727). Blue and red spectra show the observed and each color corresponds to observed channels (left axis). The black spectrum shows the modeled spectrum (right axis, Narayan et al., 2019).

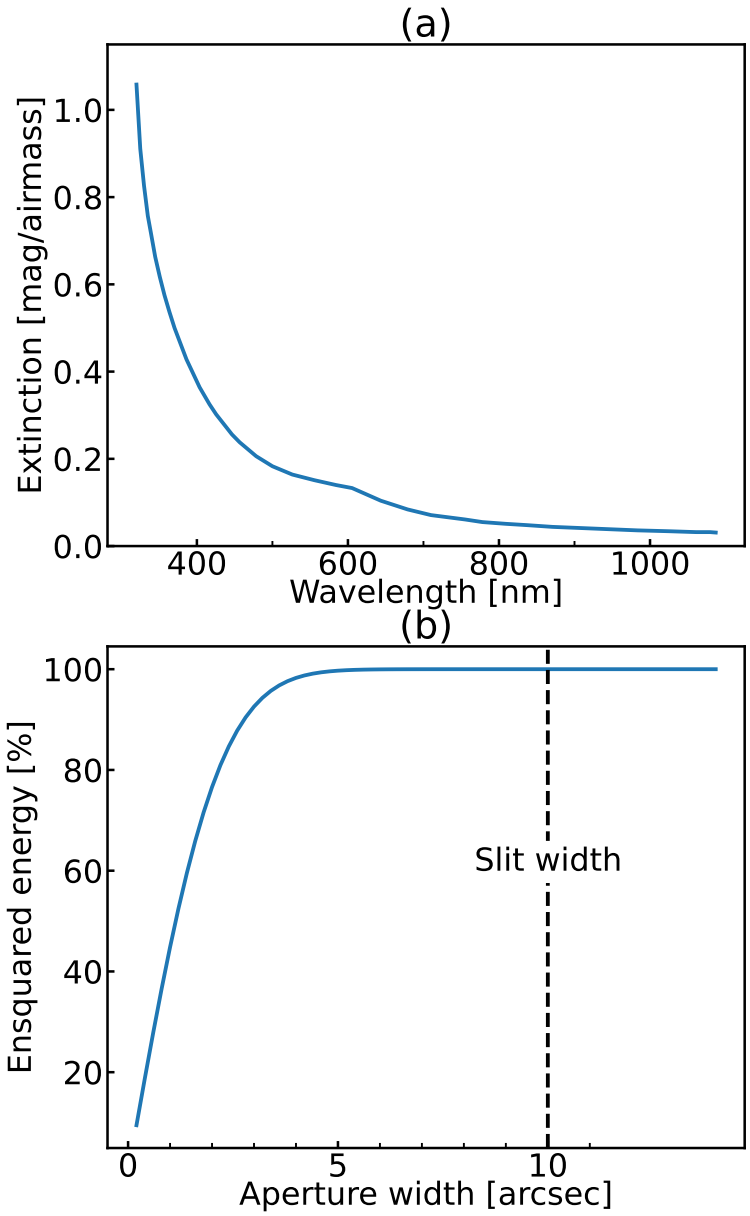

Figure 3.7: The information of calculation of conversion factor. (a) : Airmass extinction curve of the Palomar Observatory (Hayes & Latham , 1975). (b) : The ensquared energy of the standard star SDSSJ0727. The PSF of the star was assumed to be a two-dimensional Gaussian. The position of the 10" slit used in this observation is indicated by a dashed line.

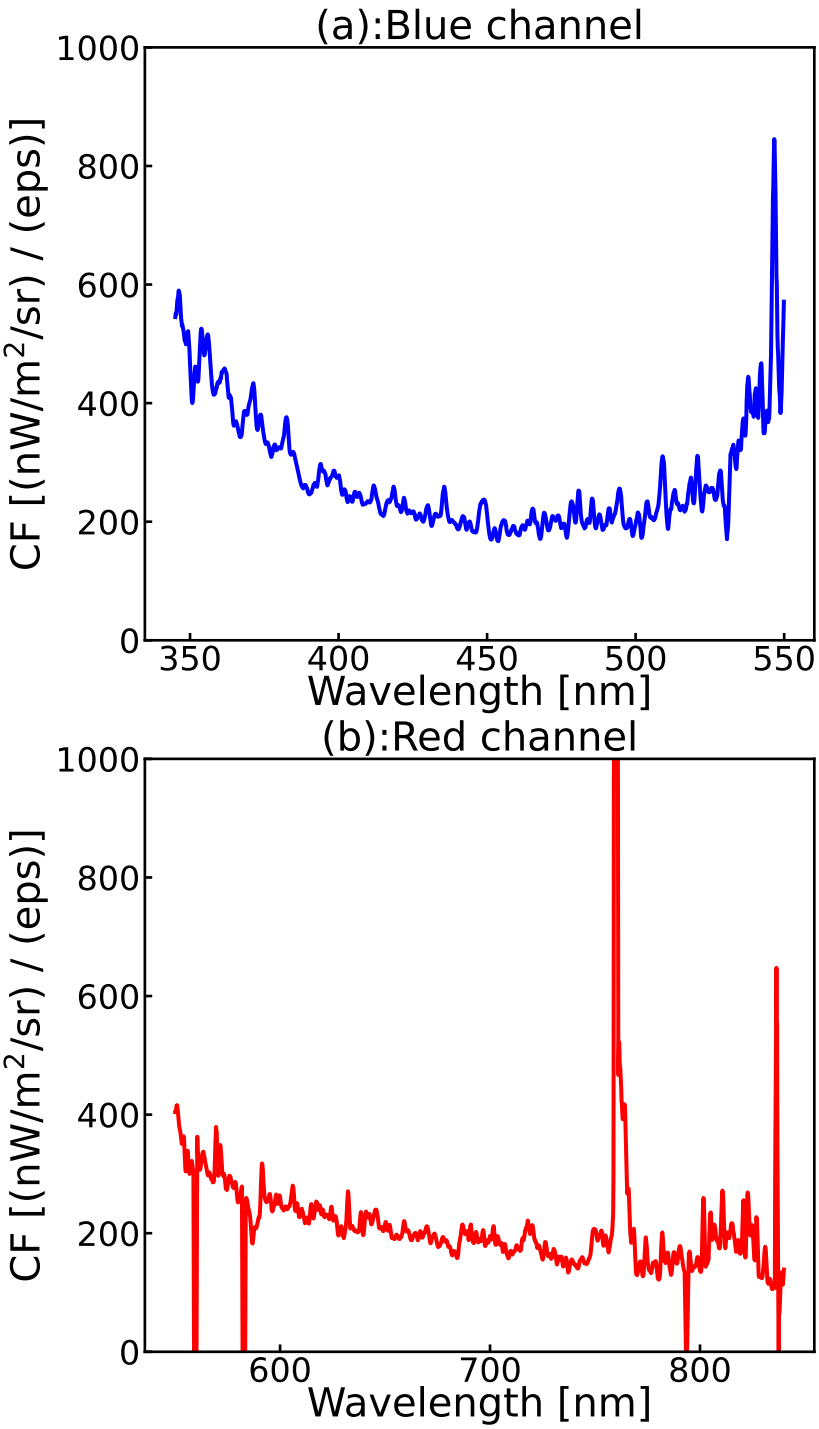

Figure 3.8: Flux calibration factors calculated by equation 3.2. FIgure (a) shows the blue channel and FIgure (b) shows the red channel.

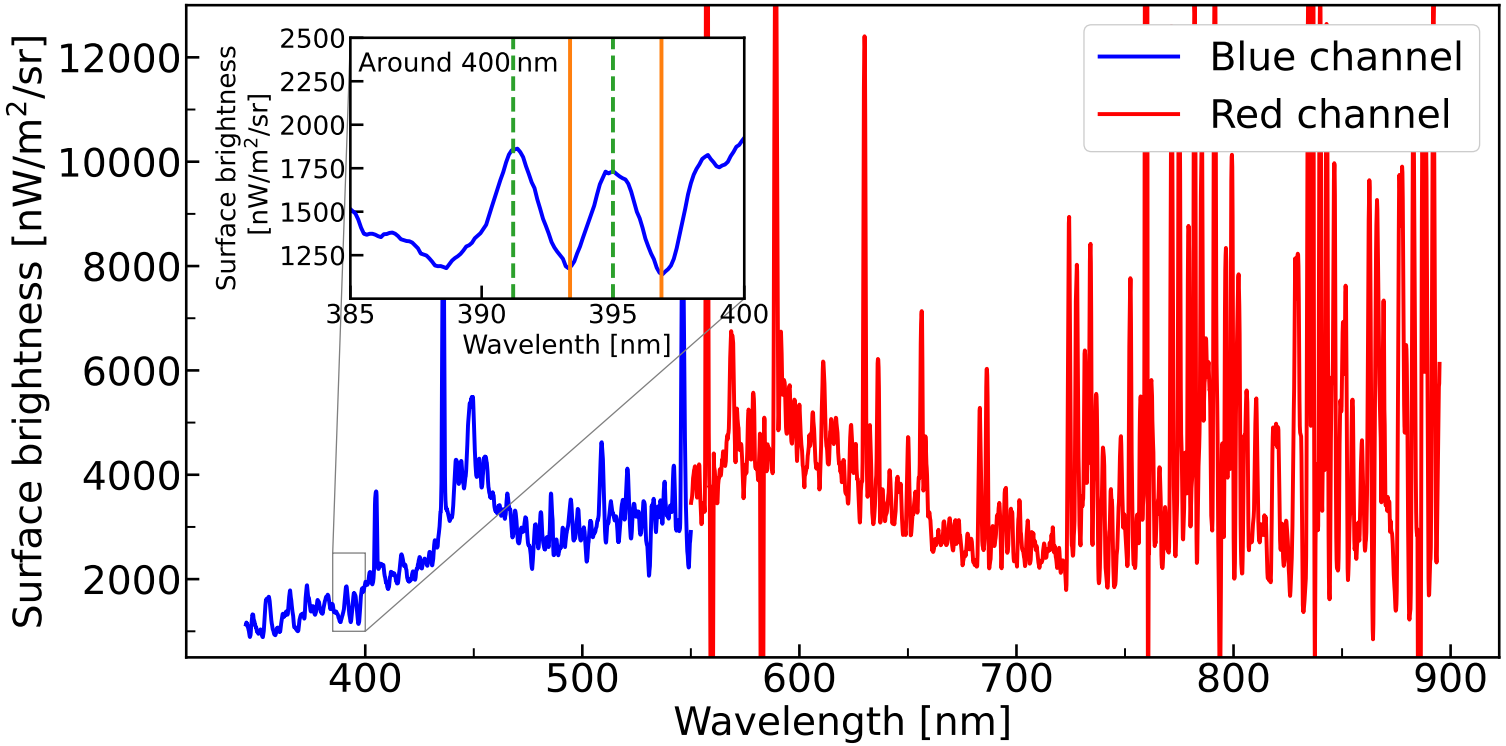

Figure 3.9: Night-sky spectrum in "Elon82Step6". Blue and red lines show the spectrum obtained from DBSP blue and red frame. we also show the spectrum zoomed around the 400 nm, which are around strong Fraunhofer lines, at the left-top side. The orange lines are CaIIλ 393.3 nm and CaIIλ 396.8 nm. The surrounding airglow emission is shown in green dashed lines, which are emission lines due to N_2^+ (391.2 nm) and O_2 (395.0 nm).

Chapter 4

Results

4.1 Creation of spectrum template

As shown in figure 3.9, the observed night-sky spectra are dominated by atmospheric light above 450 nm. On the other hand, there are two valley shapes around the Ca II $\lambda\lambda 393.3, 396.8$ nm absorption lines, which are strong Fraunhofer lines (the orange lines in the zoomed image in figure 3.9). However, there are also airglow emission lines, N_2^+ and O_2, in the vicinity (the green-dashed lines in the zoomed image in figure 3.9), and these components may cause large uncertainty in the ZL continuum. Therefore, since the night-sky brightness ($\lambda I_{\rm NS}$) is linear combination of airglow ($\lambda I_{\rm Air}$), ZL ($\lambda I_{\rm ZL}$), DGL ($\lambda I_{\rm DGL}$), integrated starlight (ISL,$\lambda I_{\rm ISL}$) and other isotropic components including EBL ($\lambda I_{\rm Res}$) as in equation 4.1, we created a template for each component.

$$\lambda I_{\rm NS} = \lambda I_{\rm Air} + \lambda I_{\rm ZL} + \lambda I_{\rm DGL} + \lambda I_{\rm ISL} + \lambda I_{\rm Res} \tag{4.1}$$

4.1.1 Airglow spectral template

The airglow spectra vary in intensity depending on the conditions of the atmosphere of Earth, which in turn depend on the direction and time of observation. Therefore, it is difficult to create an airglow spectrum for each observed data. Where the modeled ZL brightness calculated by Kelsall et al. (1998) and Kawara et al. (2017) align, we compare the observed data across two different fields. The difference in the spectrum of these two fields is used as a standard airglow spectral template. By taking the difference between

the two observed fields, it is possible to remove the ZL, DGL, starlight, and EBL components from the night-sky brightness. In addition, assuming that the spectral shape of airglow is constant on average, the spectrum of the difference is regarded as the airglow spectral template.

To derive the spectral template of the airglow, we chose the two fields with similar brightness of the celestial emission components, mainly of the ZL brightness. The ZL brightness at 400 nm was calculated by interpolating the ZL brightness in the visible bands in Kawara et al. (2017) with the solar spectrum and determining the absolute brightness with the Kelsall model (Kelsall et al., 1998) using the Python library *Zodipy* (San et al., 2022), as we show the black plots in figure 4.1. The selected fields for difference are the high-brightness data indicated by the green circle and the low-brightness data indicated by the three red circles in figure 4.1. The model ZL brightness in the selected fields are in agreement within 10 nW m^{-2} sr^{-1}, and the differences of 500 nW m^{-2} sr^{-1} between the fields are certainly due to the airglow. The spectral template of the airglow shown in figure 4.2 was obtained by averaging the brightness differences. This spectral template has the same spectral feature of Broadfoot and Kendall (1968) and Krassovsky et al. (1962).

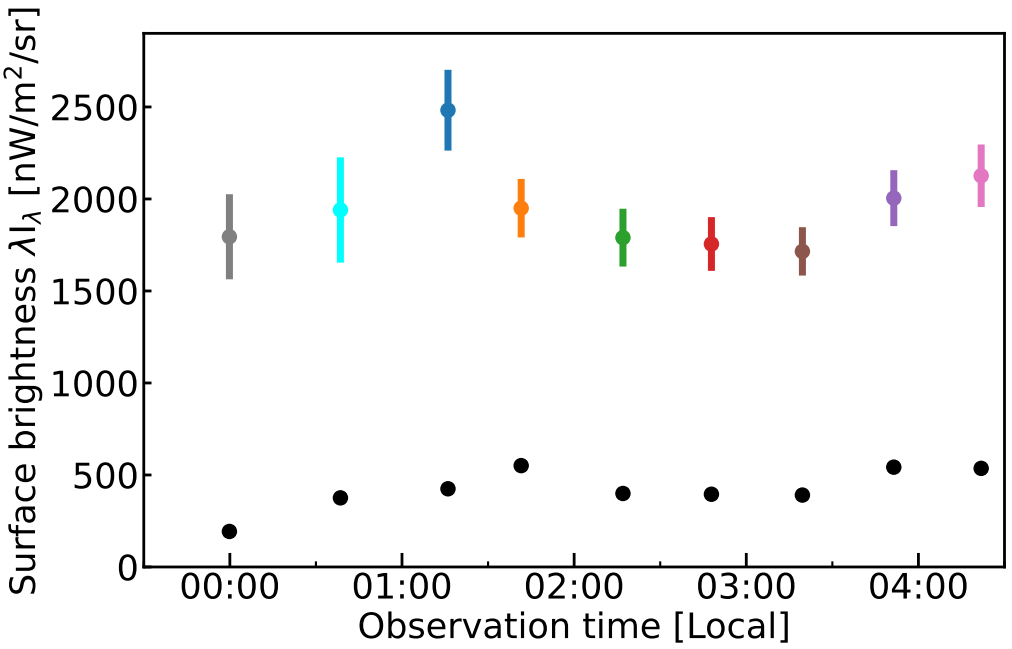

Figure 4.1: Time variation of observed night-sky (color plots) and ZL brightness expected from the Kelsall model (black plot). The night-sky brightness is the average brightness from 400 nm to 403 nm. Airglow template was obtained by subtracting the averaged spectrum in the red circles from that in the green circle, at each wavelength.

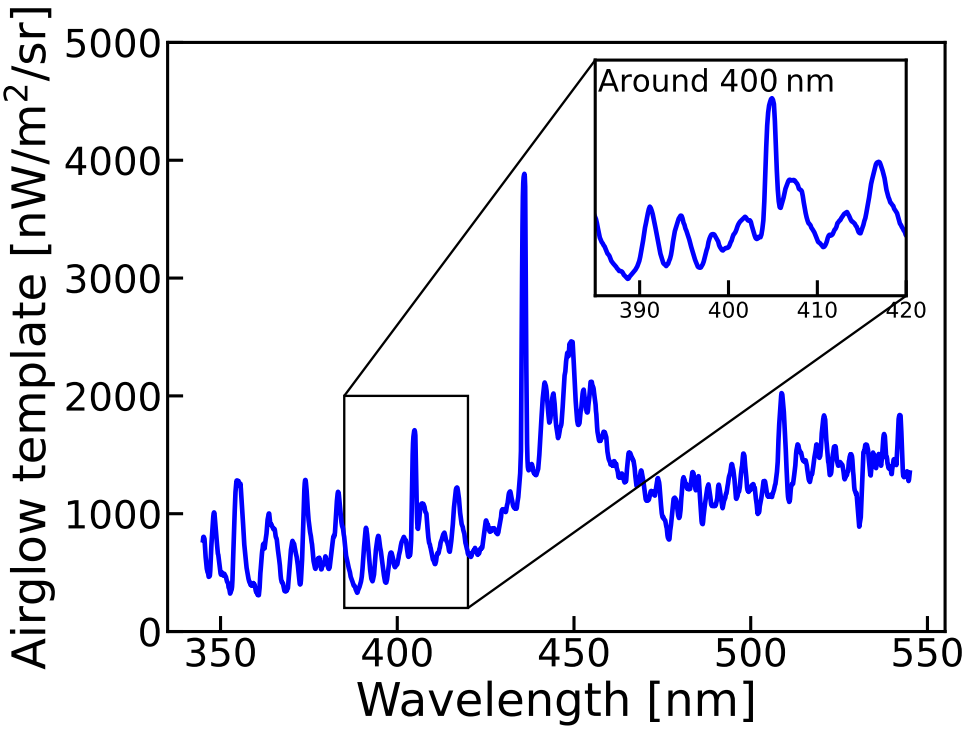

Figure 4.2: The airglow spectral template. we also show the spectrum zoomed around 400 nm at the right-top side. The calculation method of this template is shown in section 4.1.1.

4.1.2 ZL template spectrum

Although the ZL spectrum is redder than the solar spectrum due to the optical properties of IPD (Leinert et al., 1998), the ZL spectrum can be assumed to be identical to the solar spectrum in a narrow spectral range around the Fraunhofer line. The solar spectrum used in this study was calculated using MODTRAN (Berk et al., 2014, 2015).

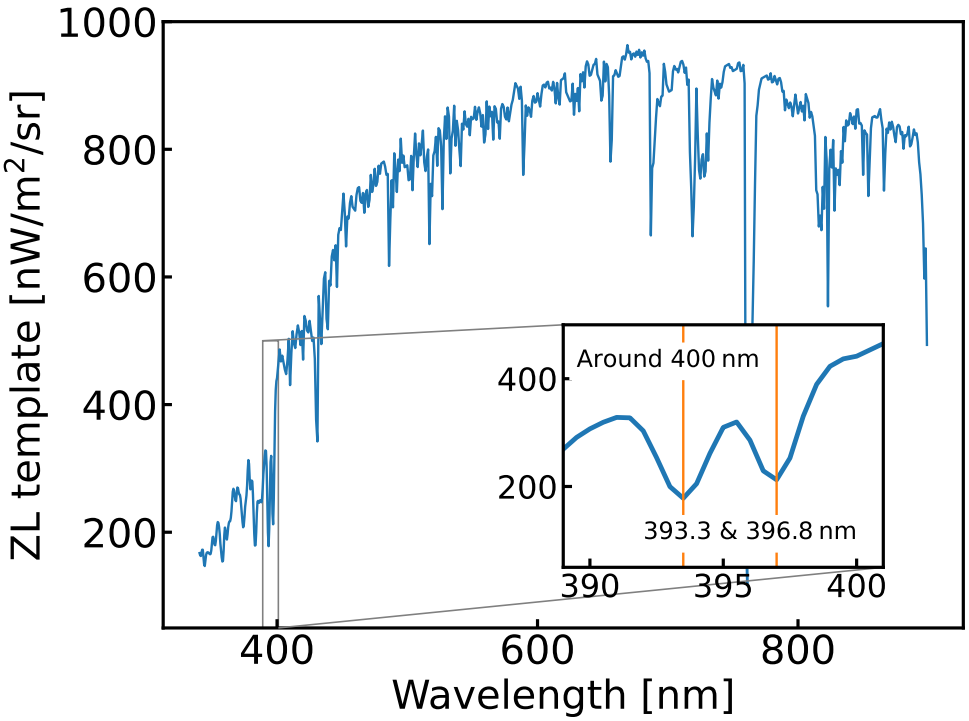

Figure 4.3: The ZL spectral template calculated by MODTRAN. The insert figure shows around Ca II $\lambda\lambda$ 393.3, 396.8 nm. The spectral shape is the same as the solar spectrum.

4.1.3 DGL template spectrum

The DGL brightness, which is starlight scattered by interstellar dust, is correlated with far-infrared emission, which is the thermal radiation from the interstellar dust (e.g. Onishi et al., 2018). Therefore, we calculated the DGL brightness ($I_{\rm DGL}$) in each field based on the SFD 100 μm intensity ($I_{100\mu{\rm m}}$, Schlegel et al., 1998), we show an example in figure 4.4 (a) and all fields in figure G.2 in appendix G, with the linear correlation as

$$\lambda I_{\rm DGL} = a I_{100\mu{\rm m}}, \tag{4.2}$$

We adopted the correlation coefficient a from Kawara et al. (2017) and the spectral shape of the DGL was taken from Mattila et al. (2017). The ratio of DGL and $I_{100\mu{\rm m}}$ spectrum is shown in figure 4.4 (b). The DGL brightness at 400 nm calculated by this method is shown in table 4.1. The

uncertainty of the DGL brightness is calculated by propagating the difference between SFD 100 μm intensity (Schlegel et al., 1998) which we employed and IRIS 100 μm intensity (Miville-Deschênes & Lagache , 2005) and the error of correlation coefficient a from Kawara et al. (2017). We show the uncertainty of the DGL brightness in "Uncertainty" of table 4.1.

Table 4.1: The DGL brightness at 400 nm.

Field	DGL λ =400 nm	Uncertainty
	units : nW m^{-2} sr^{-1}	
WISE-J0301	47.9	10.1
Elon66Step17	196.9	14.4
Elon66Step28	280.8	19.0
Elon66Step29	299.4	36.8
Elon66Step30	319.2	36.6
Elon82Step6	196.3	11.4
Elon82Step7	266.0	9.8

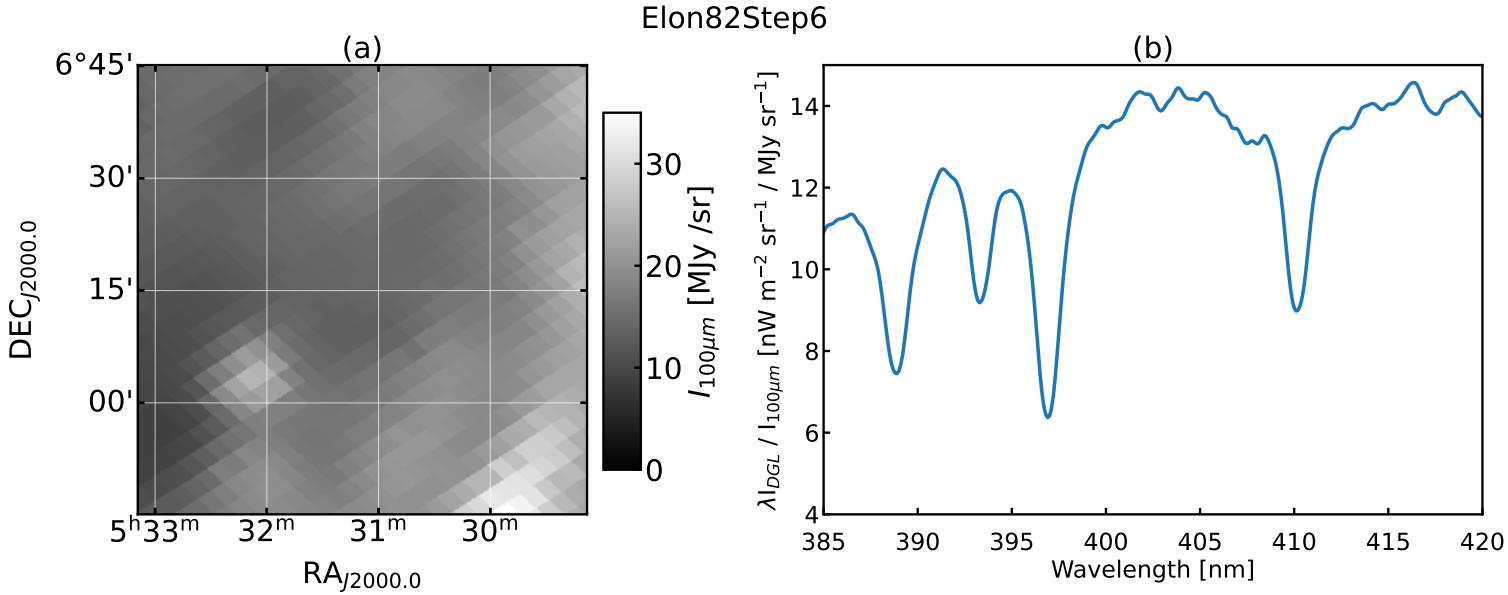

Figure 4.4: (a): An example of 100 μm brightness $I_{100\mu\mathrm{m}}$ map (Schlegel et al., 1998). The field is Elon82Step6. (b); $I_{\mathrm{DGL}}/I_{100\mu\mathrm{m}}$ spectrum. The DGL component of each field is this spectrum multiplied by the 100 μm brightness $I_{100\mu\mathrm{m}}$ by Schlegel et al. (1998) [Figure (a)].

4.1.4 Integrated starlight

The bright stars are masked out from the observed images to measure the diffuse sky brightness. The ISL, which is the integrated light of stars fainter than the detection limit, should be subtracted as the diffuse light from the observed night-sky brightness. We calculated the ISL brightness for stars with the magnitude ranging from the magnitude cut, corresponding to the detection limit, down to 30 ABmag at the optical wavelength using TRILEGAL(Girardi et al., 2005; Girardi and Marigo, 2007; Girardi et al., 2012; Groenewegen et al., 2002; Vanhollebeke et al., 2009), which provides the simulated star catalog towards the specified fields.

TRILEGAL is a tool that can simulate the number of stars in the Galaxy and the spectrum of each star. The tool can simulate the amount of interstellar dust in the Galaxy, the fraction of binary stars, the position of the Sun, and the shape of the Galaxy (disk, halo, and bulge). The simulations are consistent with the 2MASS catalog and can be applied to deep ($16 < R < 23$mag) simulations such as the Chandra Deep Field South data and shallow ($V < 8$mag) Hipparcos data (Girardi et al., 2005). However, there are large errors in the direction of the Galactic center, Galactic plane, and South Galactic latitude(Girardi et al., 2005).

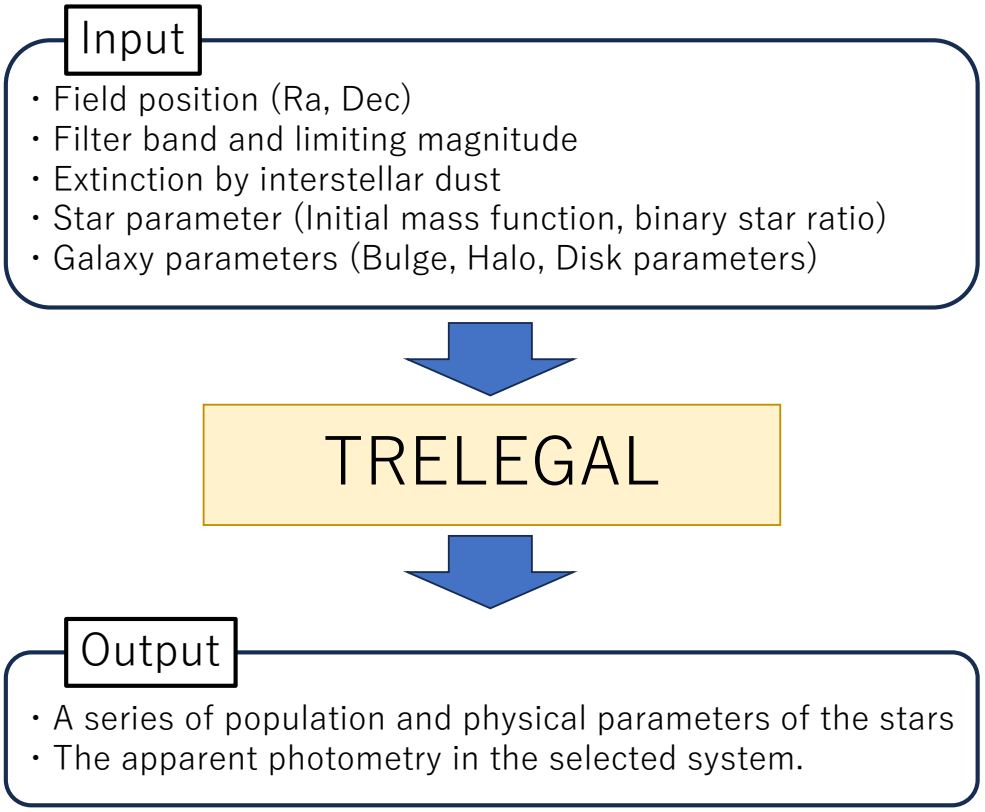

Figure 4.5: Outline of TRILEGAL

The HST bands were close to the observed wavelengths among the available wavelengths for TRILEGAL. Therefore, as substitutes for wavelengths observed in this study, we calculated the ISL brightness with HST/F390W ($\lambda = 392.4$ nm) and HST/F410M ($\lambda = 410.9$ nm). The area of this simulation is 0.5 deg^2, which is different from the area of the observed fields in this observation. Therefore, the expected star count per each magnitude $E(m)$ entering the slit was calculated by equation 4.3 for this observation.

$$E(m) = \frac{n(m)}{0.5}\Omega_{\mathrm{Slit}}. \tag{4.3}$$

$n(m)$ is the number of stars per magnitude in 0.5 deg^2 obtained in this simulation, $\Omega_{\mathrm{Slit}} = 128" \times 1"$ is the solid angle of the slit used in this observation. Figure 4.6 shows an example of the expected star count per each magnitude obtained by this method (the results in all fields are shown in figure G.3 in

appendix G).

We performed this simulation ten times for each field with the detection limit of 26 ABmag at 400 nm, which corresponds to the standard deviation of the night-sky signal. As shown in figure 4.7, the calculated brightness of the ISL is less than 0.05 nW m^{-2} sr^{-1} and significantly fainter than the night-sky brightness.

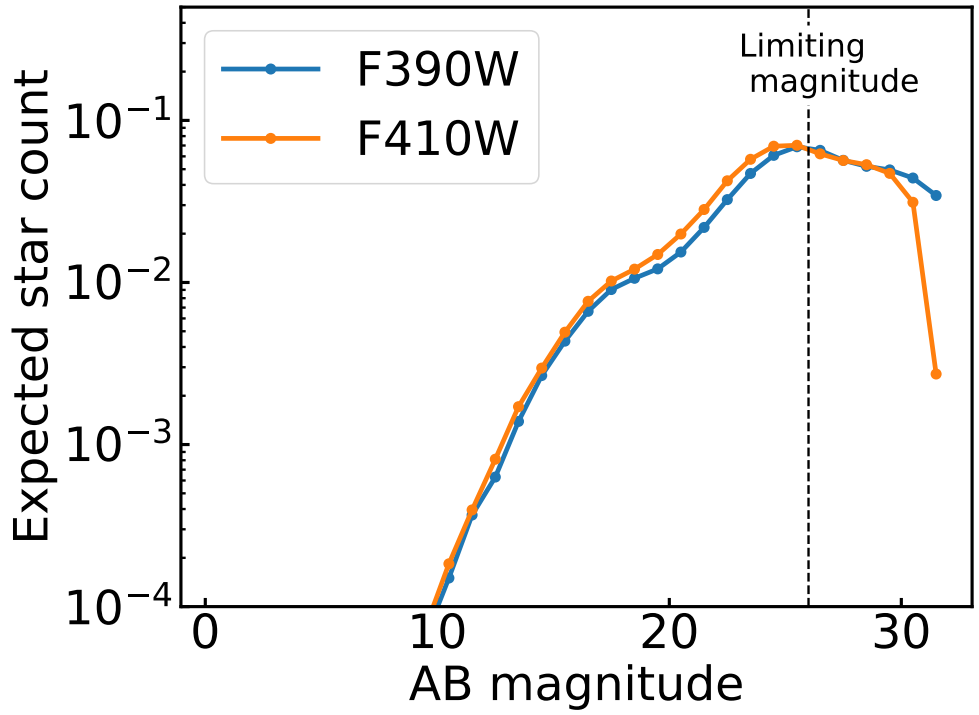

Figure 4.6: Expected value of star count at each magnitude with this observation calculated by equation 4.3. The blue and orange plots show the results of HST/F390W and HST/F410M which we substitute for wavelengths observed in this study.

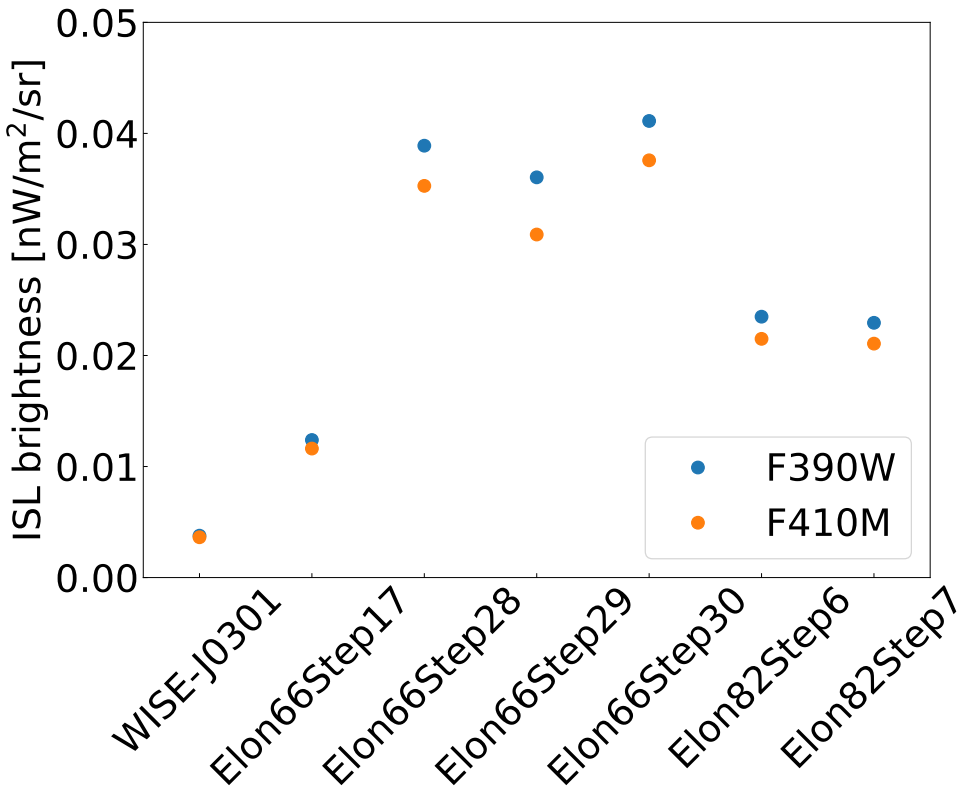

Figure 4.7: The estimated ISL brightness. Blue plots represent the results from HST/WCS3 F390W and orange plots are from F410M.

4.2 Results of the spectral fitting.

4.2.1 Results of the spectral fitting.

Using the templates for each component described in section 4.1, the observed data were fitted by equation 4.1 with chi-square analysis. The airglow and the ZL components are constant multiples of their template spectra. In addition, other isotropic components including EBL were assumed to be constant because the wavelength range is narrow and the influence of wavelength dependence of EBL is 0.48 nW m^{-2} sr^{-1} which is the below 0.1% of night-sky brightness. This component also includes a constant component of atmospheric radiation that was removed when the airglow spectral template was created.

The wavelength range for the fitting was from 385 nm to 420 nm. An example of the fitting results is shown in figure 4.8. We show all the fitting results in appendix G.

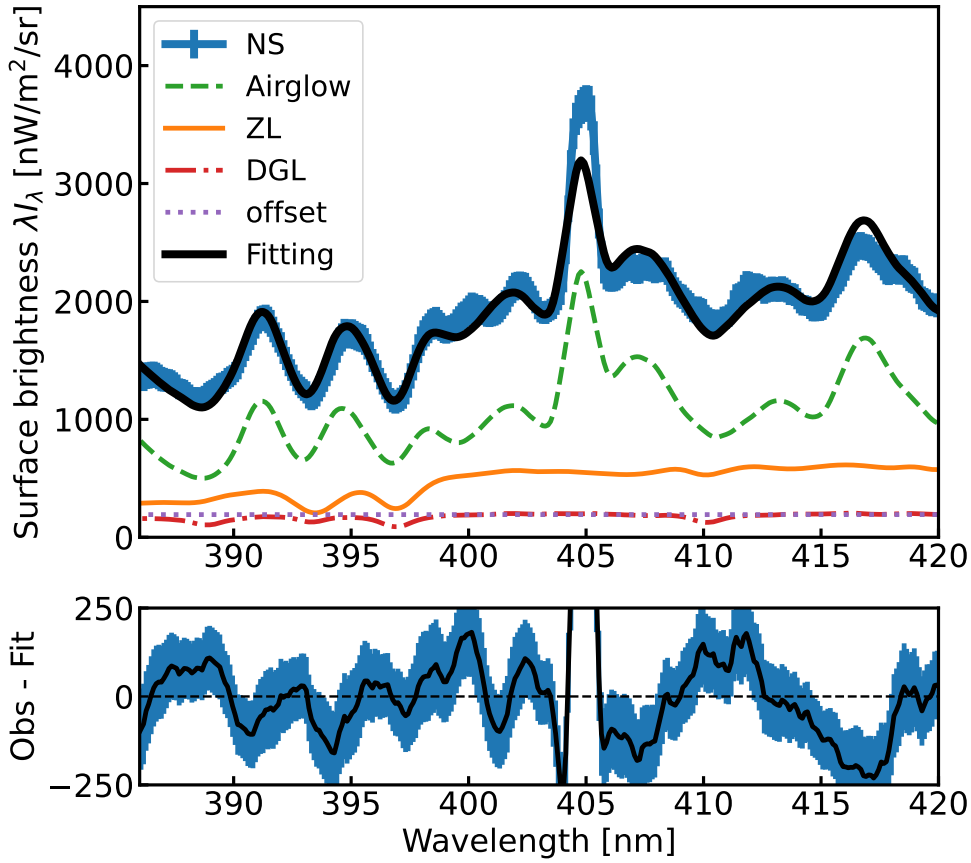

Figure 4.8: (Top): Fitting of observation data. We show Elon82Step6 as an example. The blue line shows the observed night-sky spectrum, the green dashed line shows airglow, the orange line shows the ZL, the red dash-dot line shows the DGL, the purple dotted line shows the other isotropic component with offset, and the black line shows the best-fitted spectrum. (Bottom): The residual value (NS minus Fitting in the top figure). The black line shows the difference and the blue area shows the error in the observed spectrum.

The spectral line at 405 nm is not fitted well, because it shows the time variation different from the continuum. However, the observed spectrum and the model are consistent within the error range near the Fraunhofer line (see bottom figure in figure 4.8) and are not affected by the emission lines around

the Fraunhofer line.

The reduced chi-square χ^2_ν/ν for the fitting including this emission line calculated by equation 4.4 is lower than 1.5 for all fields as summarized in table 4.2. Therefore, this fitting is accurate enough to explain the observed data.

$$\chi^2_\nu/\nu = \frac{1}{\nu}\sum_i \left(\frac{y_i - f_i}{\sigma_i}\right)^2; \tag{4.4}$$

where y_i and f_i are the i^{th} observed and modeled value, σ_i is the i^{th} error attached y_i, and ν is the degree of free defined as the number of samples minus the number of parameters.

4.2.2 Estimation of the ZL brightness and comparing the modeled ZL brightness

Based on the ZL spectrum obtained by section 4.2.1, a linear fitting was performed for 399 nm to 401 nm, where the wavelength width is narrow and the spectral shape can be assumed to be a linear function of wavelength. The results of the ZL brightness at 400 nm based on the linear fitting are shown in figure 4.9 and table 4.2. The uncertainty of the ZL brightness by fitting ($\sigma_{\rm fit}$, shown in Err1 of Table 4.3) was obtained by propagating the scaling factor of the solar spectrum and the fitting error for continuum. The result is compared to the with the model calculations same as figure 4.1. The observed ZL brightness is similar to the model calculations except for the Elon66tep7, which shows a large difference exceeding the error bar. Possible reasons for the difference are discussed in section 5.

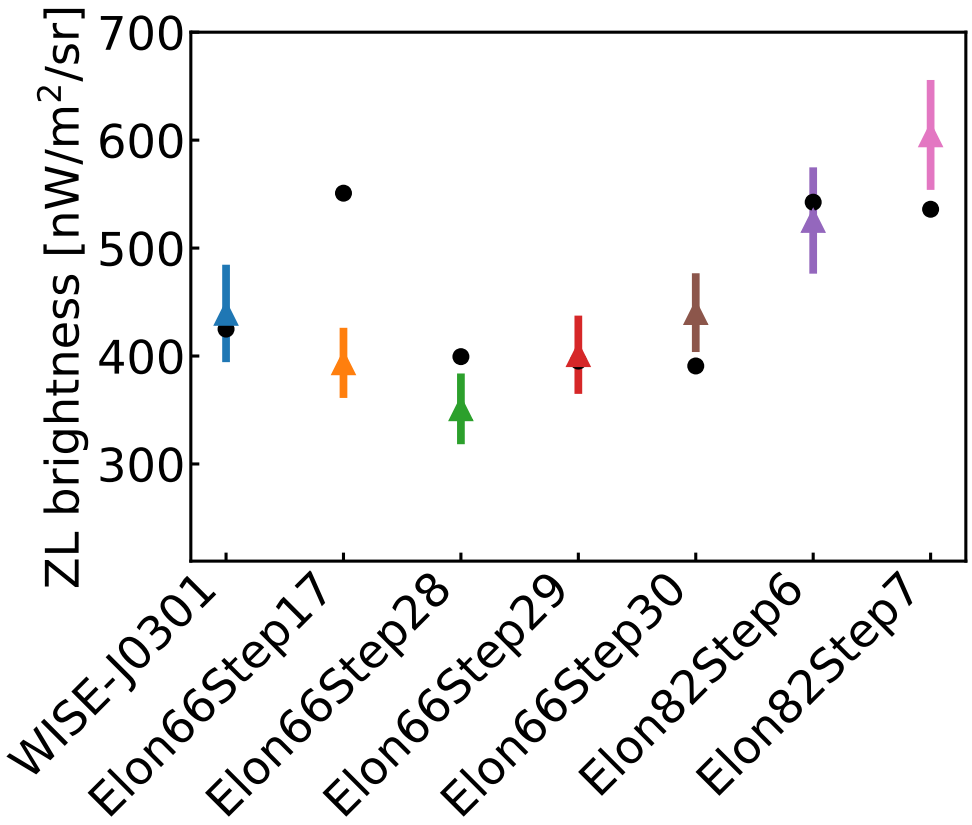

Figure 4.9: The ZL brightness at 400 nm. Color triangle plots are observed results and the error bar attached to each data is the total statics uncertainty in Err4 of table 4.3. Black circle plots are the modeled ZL brightness (Kawara et al., 2017; Kelsall et al., 1998). The fields indicated on the horizontal axis are arranged in chronological order of observation time.

Table 4.2: Fitting result at 400nm.

Field	Airglow	ZL	Difference[6]	reduced chi-square
	unit : nW m^{-2} sr^{-1}			
WISE-J0301	1773.9	441.6	20.9	0.69
Elon66Step17	1212.5	395.6	-148.1	0.98
Elon66Step28	1028.7	352.8	-42.0	1.32
Elon66Step29	950.9	403.1	12.3	1.27
Elon66Step30	885.5	442.3	56.0	1.44
Elon82Step6	1019.7	528.1	-6.3	1.29
Elon82Step7	1003.7	607.8	79.7	1.23

[6] The observed ZL brightness(color circle plots in figure 4.9) minus the modeled ZL brightness(black plots)

4.3 Uncertainty of the ZL brightness

4.3.1 Uncertainty from the wavelength range of fitting.

The derived ZL brightness depends on the wavelength range for the fitting by equation 4.1 as shown in figure 4.10. While the minimum wavelength was fixed to 385 nm, the maximum one was changed to see the dependence (the results for the observed fields are shown in appendix G). The figure shows that for $\lambda < 415$ nm, the observed ZL brightness has a large variation with the maximum wavelength. On the other hand, in the range from 415 nm to 435 nm, the estimated ZL brightness is stable within 10% and we defined the uncertainty from the variation of wavelength range (see Err2 in table 4.3). In addition, based on this result, we chose 420 nm as a fiducial value of the maximum wavelength in our fitting.

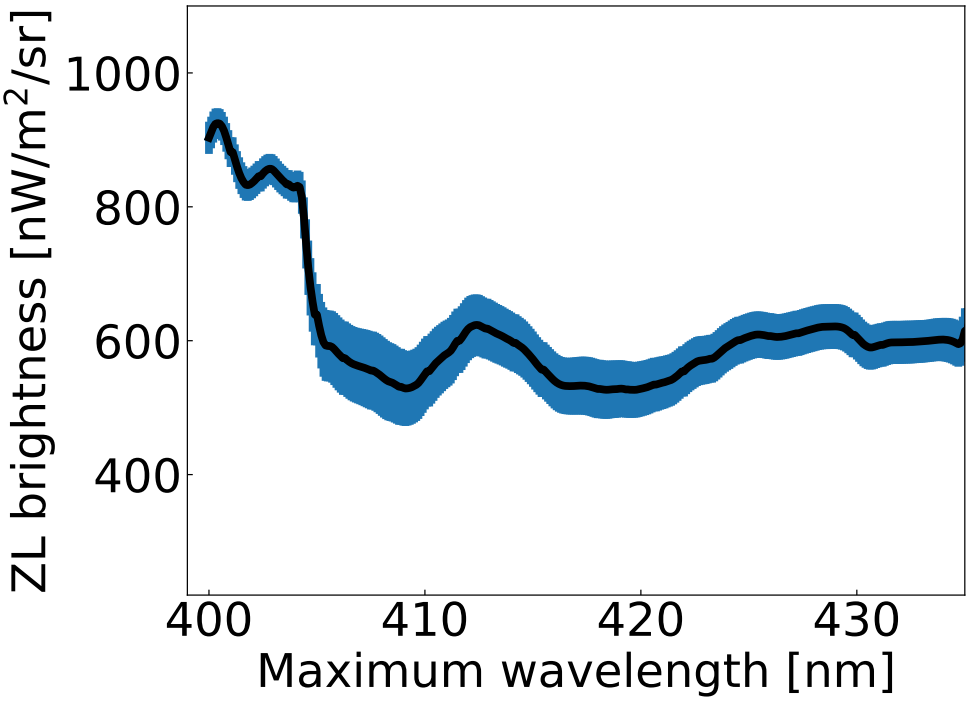

Figure 4.10: An example of the variation of the ZL brightness for different maximum wavelengths used to derive ZL brightness. The field is Elon82Step6. The horizontal axis is the end of the fitting wavelength. Error bars (blue region) are values estimated by the standard error produced by each fitting.

4.3.2 Uncertainty from the airglow spectral template.

The airglow spectral template $M_{\lambda,\mathrm{Air}}$ is obtained by differing the observed data. Therefore, the error of the airglow spectral template as a function of the wavelength($\delta_{Air,\lambda}$) is obtained by propagating the error of each data. Hence, to account for these factors, we conducted a Monte Carlo simulation where we randomly varied the airglow spectral template according to equation 4.5.

$$M'_{\lambda,\mathrm{Air}} = M_{\lambda,\mathrm{Air}} + \delta_{\lambda,\mathrm{Air}} R_\lambda \tag{4.5}$$

The parameters of the equation 4.5 are as follows. $M'_{\lambda,\mathrm{Air}}$ is the airglow spectral template after the variation and R_λ is a random number generated for each wavelength following Gaussian distribution with a mean of 0 and a standard deviation of 1.0. Based on this, we calculated 200 sets of $M'_{\lambda,\mathrm{Air}}$ such

that they fall within the range of $M_{\lambda,\mathrm{Air}} \pm \delta_{\lambda,\mathrm{Air}}$ with a 95% confidence level. For each realization of the simulation, we employed the same method as in section 4.2.1 to derive the observed ZL spectrum. We show an example of the resulting histogram in figure 4.11 (in figure G.6 in appendix G, we show all results of this analysis). The uncertainty of the ZL brightness is derived from the standard error of the histogram. As a result, the uncertainty introduced by the airglow spectral template is about 1.5 nW m^{-2} sr^{-1} (see Err3 in table 4.3).

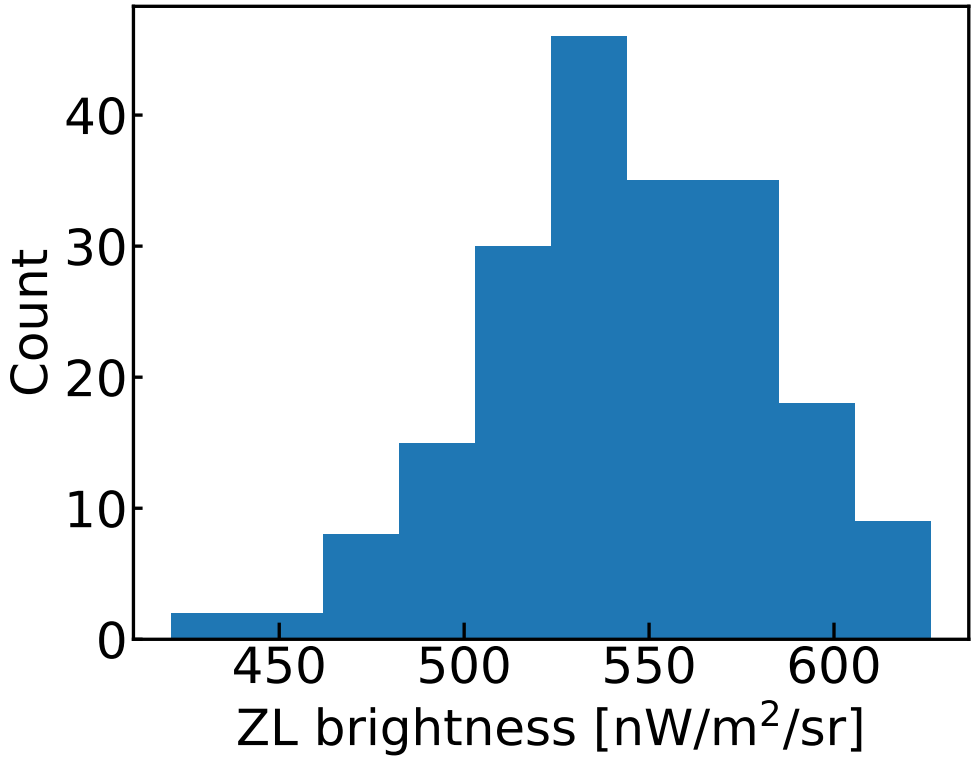

Figure 4.11: An example of the resultant of the Monte-Carlo simulation to indicate the uncertainty of the ZL brightness at 400 nm. The field is Elon82Step6. The histogram represents variations in ZL brightness (200 samples for each field) obtained by altering equation 4.5 within the airglow spectral template. The result of all fields is shown in figure G.6.

As a result of these evaluations, the total statistical error (σ_{stat}) of the

ZL brightness is determined as

$$\sigma_{\rm stat} = \sqrt{\sigma_{\rm fit}^2 + \sigma_{\rm wv}^2 + \sigma_{\rm airglow}^2}, \tag{4.6}$$

where $\sigma_{\rm fit}$ is the fitting error, $\sigma_{\rm wv}$ is the error from the wavelength range for the fitting in section 4.3.1, and $\sigma_{\rm airglow}$ is the error from the airglow spectral template. The resultant uncertainties of the ZL brightness are shown in the Err4 column of table 4.3

4.3.3 Uncertainty from the DGL brightness.

We estimate the uncertainty in the ZL brightness from the multicomponent fit for the upper and lower bounds of the uncertainty in the DGL brightness shown in table 4.1. The results are shown in the Err5 column of table 4.3.

The uncertainty in the ZL brightness from the EBL uncertainty is already taken into account as an offset component in the multicomponent fit.

Table 4.3: Uncertainty of the observed ZL brightness.

Field	Err1[7]	Err2[8]	Err3[9]	Err4[10]	Err5 [11]
	unit : nW m^{-2} sr^{-1}				
WISE-J0301	± 37.4	± 25.2	± 4.6	± 45.3	+4.5/-4.5
Elon66Step17	± 30.4	± 11.3	± 3.1	± 32.6	+3.9/4.0
Elon66Step28	± 30.4	± 12.1	± 2.7	± 32.8	+3.9/-4.9
Elon66Step29	± 32.8	± 15.3	± 2.5	± 36.3	+12.6/-12.5
Elon66Step30	± 33.5	± 14.5	± 2.3	± 36.5	+10.6/-16.1
Elon82Step6	± 36.4	± 33.2	± 2.7	± 49.3	+2.5/-2.5
Elon82Step7	± 37.0	± 35.0	± 2.7	± 51.0	+0.2/-0.2

[7] Fitting error
[8] Uncertainty from wavelength range (see section 4.3.1)
[9] Uncertainty from airglow template error (see section 4.3.2)
[10] Total statistical error calculated by equation 4.6
[11] Uncertainty from the DGL brightness (see section 4.3.3).

4.4 Separation of the airglow and ZL

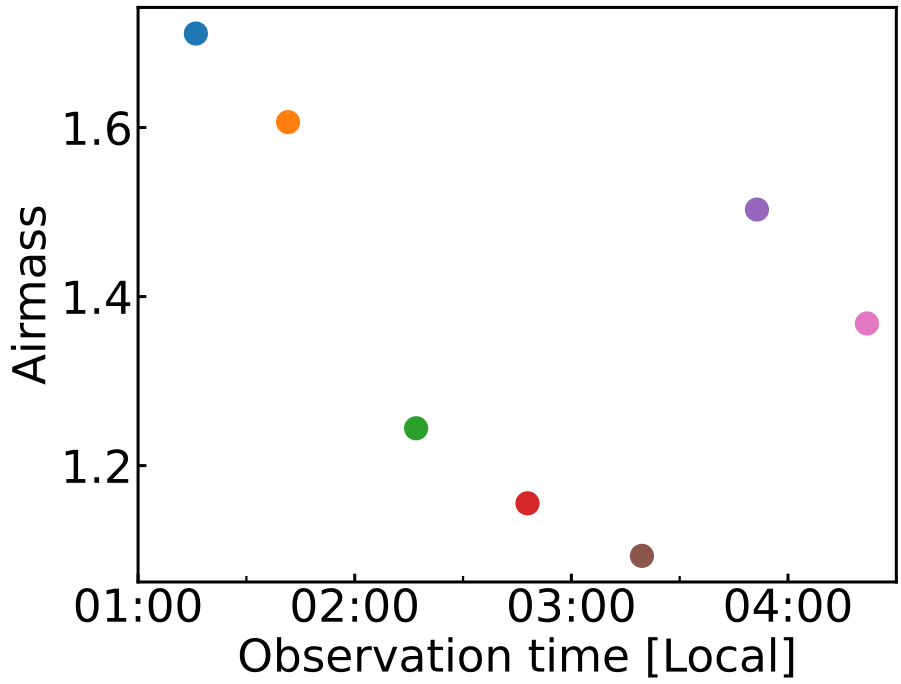

Figure 4.12: The time variation of airmass in this observation as shown in table 2.2. As the observation time progresses and becomes later, it is noticeable that the airmass values increase, indicating a significant correlation between observation time and airmass in this observation.

The airglow spectrum and intensity may vary with the local time of the observations and airmass of the line of sight, so we were careful to ensure we successfully separated the airglow component from other components. In figure 4.12, we showed the airmass as a function of local time during the observations. To assess whether we have successfully removed the airglow component from the current observation data, we compared the fitted airglow and ZL brightness with the observational conditions. The results are presented in figure 4.13. In figure 4.13 (a), the brightness of both airglow and ZL is shown with respect to observation time. It is evident that the airglow becomes dimmer as time while ZL shows no dependence on the time. In figure 4.13 (b), the airglow and the ZL brightness are plotted against airmass. The airglow becomes brighter as airmass increases, while ZL brightness does

not exhibit a similar trend. Thus we conclude the airglow and ZL are clearly separated and that the ZL measurements are not significantly affected by the airglow.

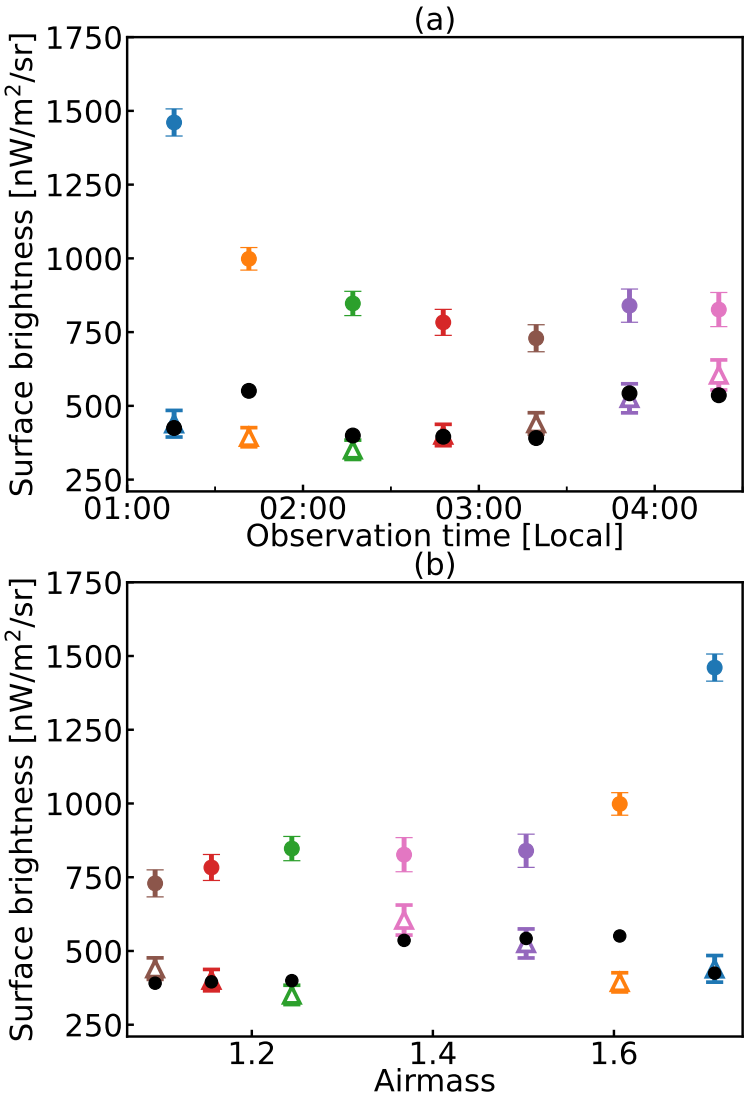

Figure 4.13: The dependency of the resultant brightness on observational conditions. The filled circle with the error bar indicates airglow, the open triangle indicates ZL brightness and the black circle indicates the modeled ZL brightness (Kelsall et al., 1998) and (Kawara et al., 2017). Error bars on each plot are total statistical error shown in Err4 of table 4.3 . Observation time and airmass are shown in table 2.2

Chapter 5

Discussion

5.1 Difference of observed and modeled ZL brightness

The observed ZL brightness at Elon66Step17 is dimmer than the prediction from the modeled ZL brightness by Kelsall et al. (1998) and Kawara et al. (2017). We considered three possible causes for the discrepancy. Figure 4.13 shows the time variation and airmass dependence of the airglow brightness during the observations. It is apparent that the airglow brightness in the Elon66Step7 field does not deviate from the time and airmass correlations of the other fields. Therefore, the overestimate of the airglow is not plausible as the cause. In addition, the uncertainty of the DGL brightness in Elon66Step17 is 14.4 nW m^{-2} sr^{-1} (see table 4.1). Therefore, the difference in the observed and modeled ZL brightness cannot be explained by the uncertainty of DGL. The nature of IPD may be the cause of the discrepancy. Figure 5.1 shows the dependence of the observed data on ecliptic longitude (a) and solar elongation (b). The ZL distribution at 400 nm is possibly different from that at 1250 nm, at which the ZL model is constructed, due to the light scattering properties of IPD such as albedo and phase function. In general, the solar-elongation dependence of the ZL is similar to the scattering phase function, while the ecliptic latitude dependence strongly reflects the distribution of IPD, because the ZL brightness is dominated by IPD near the earth. Thus, there exists the spatial variation of the albedo or/and the phase function of IPD so that the scattered light is enhanced on the ecliptic plane only, that can be the cause of the discrepancy between the observed data

and the model at the ecliptic latitude of zero as seen in figure 5.1(a) and the extraordinary solar-elongation dependence in figure 5.1(b). Previous studies have suggested the existence of the spatial variation of the dust property due to different origins of IPD in between the high latitude regions and on the ecliptic plane (Takahashi et al., 2019).

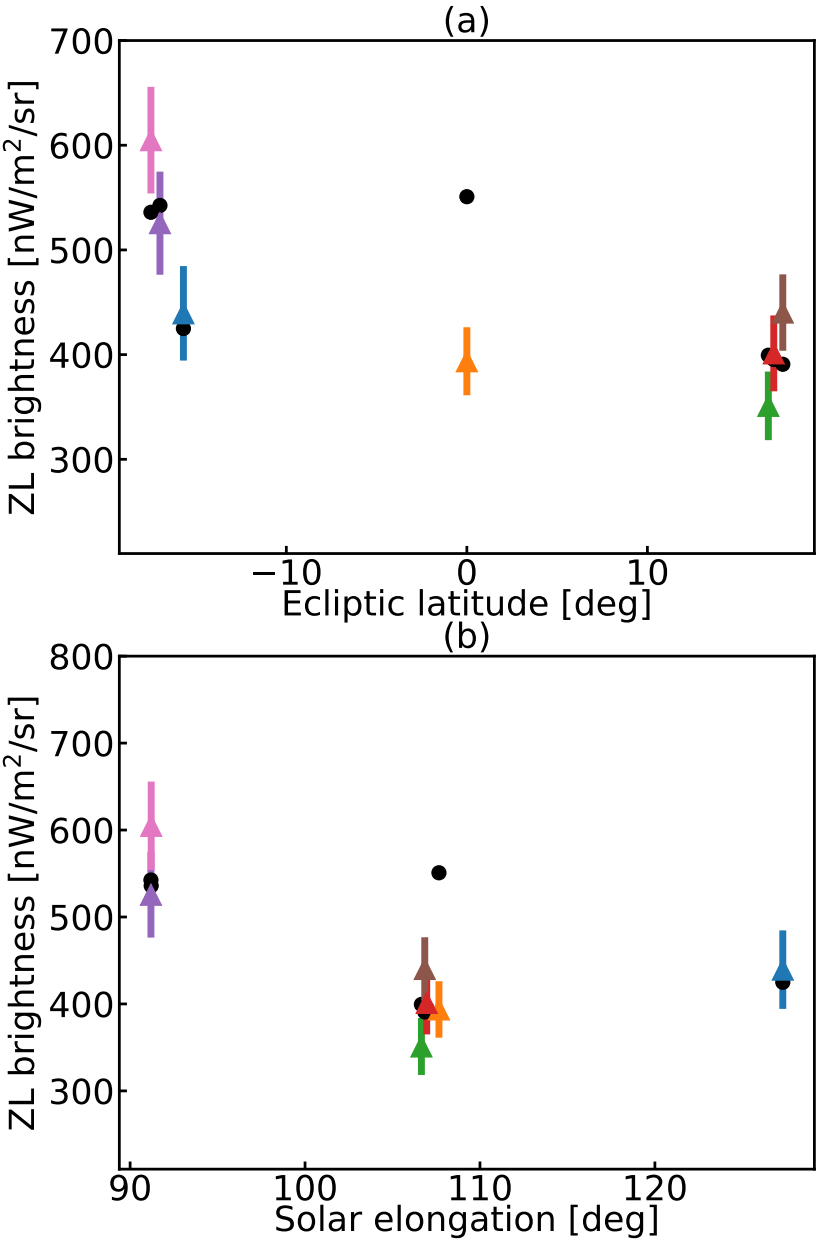

Figure 5.1: The observed ZL brightness for the observed direction, showing the dependence on ecliptic latitude (a) and solar elongation (b). The color of the plots is the same as in figure 4.9. Ecliptic latitude and solar elongation are shown in table 2.2

5.2 Future work

Through this study, we were able to separate the ZL brightness from the shape of the Fraunhofer lines in the night sky spectrum with an accuracy that agrees within the error range with the modeled ZL brightness estimated by Kelsall et al. (1998) and Kawara et al. (2017). However, the uncertainty of the observed ZL brightness in this study is 20%. In order to eliminate this uncertainty, it is necessary to conduct long-time observations of specific fields. This is expected to enable us to extract the ZL component with high accuracy by capturing the variation in the spectral shape of airglow with time and airmass.

When we observe the ZL brightness in space, we can ignore the effects of the airglow. However, high wavelength resolution and sensitivity are required for the spectroscopy of Fraunhofer absorption lines. Therefore, we expect future observations with telescopes that can achieve both in space (e.g. imaging Fourier spectrographs).

This observation is a joint observation with the EBL observation by the Spitzer Space Telescope. Therefore, we can estimate the EBL by measuring the brightness of the ZL in the Spitzer/IRAC wavelength bands at 3600 nm and 4500 nm, and subtracting the ZL from the observed data.

Chapter 6

Summary

We conducted spectroscopic night-sky observations towards low-ecliptic latitude fields with a high-resolution to resolve the Fraunhofer absorption lines of ZL in the visible wavelength region, in order to measure the absolute brightness of ZL from the line depth assuming the ZL spectrum is identical to the solar spectrum in a narrow wavelength range around the spectral lines. The observed night-sky spectra above 450 nm were mostly composed of airglow, but there were shapes of absorption lines around 400 nm. As a result of the data fitting with the spectral templates as the multi-component emission models of the airglow, ZL, DGL, ISL, and other isotropic components including the EBL, we could clearly separate the ZL component measure the depth of the CaII $\lambda\lambda$ 393.3, 396.8 nm lines at 400 nm in the night-sky spectra in all fields. The uncertainty of the observed ZL brightness of approximately 20% arises mainly from the template error and the time variation of the airglow. Observed ZL brightness in most of the observed fields is consistent with the modeled ZL brightness calculated by combining the most conventional ZL model at 1250 nm based on the DIRBE and the observational ZL template spectrum based on the HST. The obtained ZL brightness towards the ecliptic plane is significantly dimmer than the model calculation, and we discussed the discrepancy in terms of the optical properties of IPD in the dust plane.

Appendix A

Removal of observation data affected by thin clouds

Figure A.1 shows the flux calibration factors obtained from the observations of two standard stars, SDSS J0727 and WD 1817 (modeled spectrum is by Accetta et al., 2022). The former is about two times larger than the latter in the flux calibration factor, though the weather conditions during the observations for both stars looked similar to each other. For the cause of the discrepancy, we infer that for the WD 1817 observation a small thin cloud, which could not be recognized in the observation, might be located in the field of view and the star flux was largely depleted by the water extinction. In fact, there are deeper features of water absorption lines in WD 1817 than in SDSS J0727 as shown in figure A.2. Thus we decided to use SDSS J0727 only as the standard for the flux calibration as described in section 3.5.

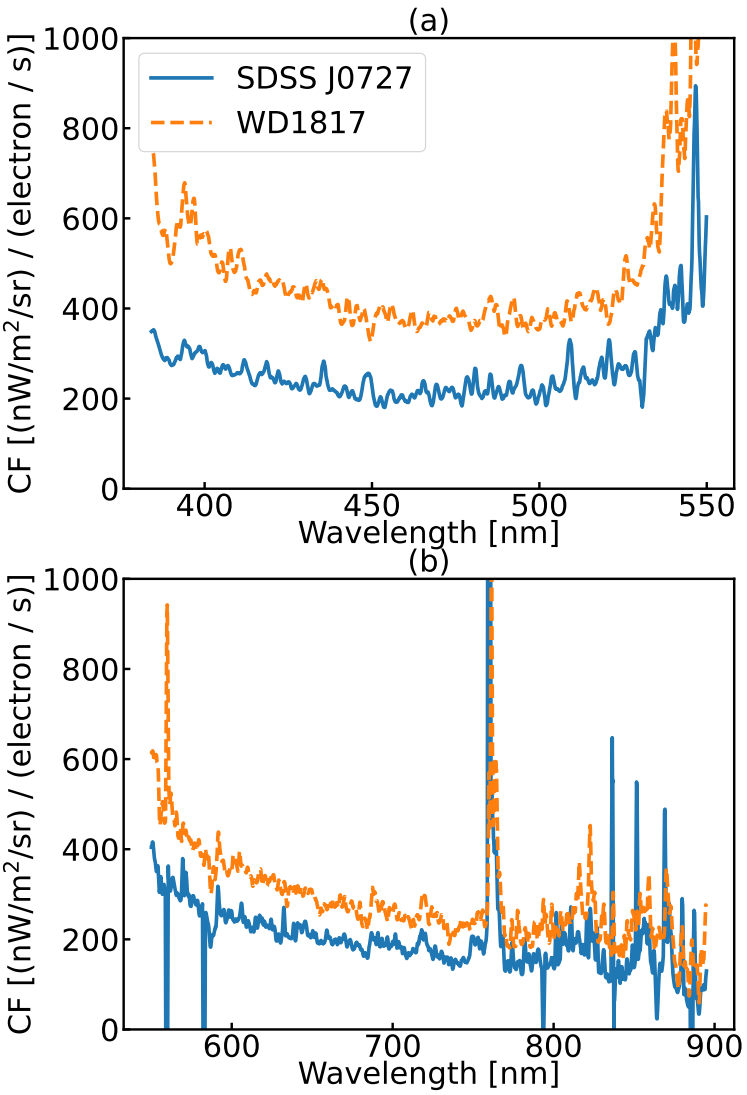

Figure A.1: Comparing flux calibration factor. (a) shows the blue channel and (b) is the red channel. Blue lines are from SDSS J0727, Oranges are from WD 1817.

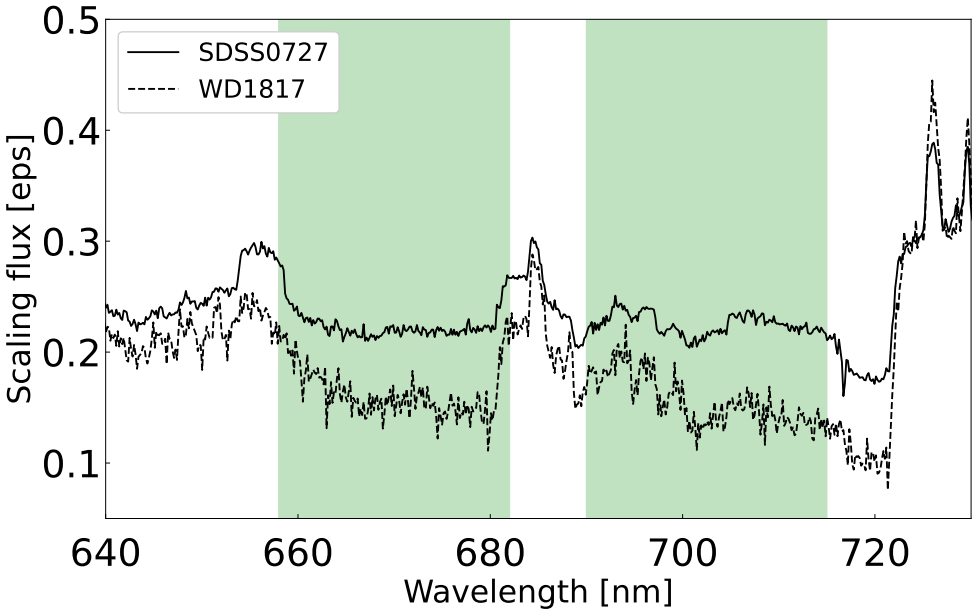

Figure A.2: Scaling spectra near water absorption line. The black solid line shows the background spectrum of SDSS J0727. The dashed shows WD 1817. Green regions are the wavelength of water absorption lines.

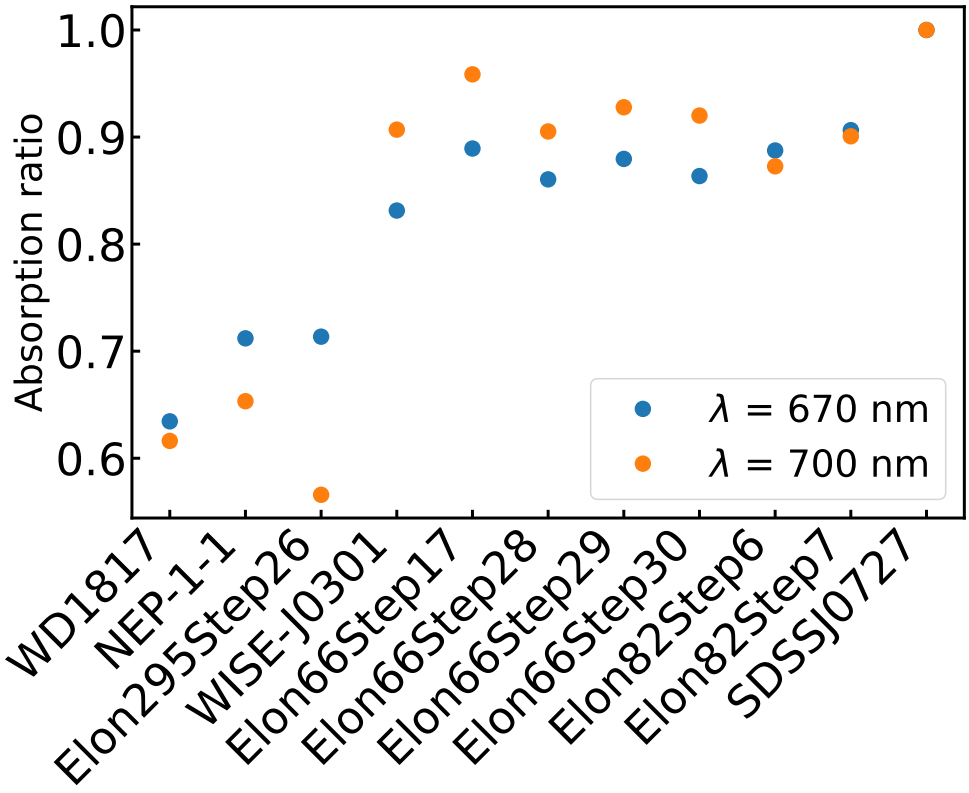

Figure A.3: The water absorption ratio for the background of SDSS J0727. The horizontal axis represents the observations arranged in chronological order, and the values for WD 1817 and SDSS J0727 are derived from the background of the standard star. The vertical axis represents the relative absorption amount with respect to SDSS J0727 at each wavelength (blue: $\lambda = 670$ nm, orange: $\lambda = 700$ nm).

Since the water absorption might also affect the night-sky spectra, we inspected the night-sky spectra of the red channel for all observations. Assuming the sky background of SDSS J0727 is not affected by the water absorption either, we calculated the ratios of the night-sky spectra, which are normalized from 500 nm to 600 nm with no water absorption, with respect to the sky background of SDSS J0727 at around 670 nm and 700 nm where the water absorption lines exist, as shown in figure A.3. As a result, we could remove the observed data before WISE-J03001 from the astronomical analysis due to infer that atmospheric conditions change between Elon295Step26 and WISE-J0301.

Appendix B

Another method of estimating ZL brightness

An example of measuring the ZL from night-sky spectra was conducted at the Boller & Chivens Spectrograph on the du Pont 2.5 m Telescope at the Las Campanas Observatory in Chili (Bernstein et al., 2002). This work used the fact that the airglow and ZL spectra do not correlate as a method to distinguish between airglow and ZL spectra in the night sky. Therefore, we used the same method to estimate the brightness of the ZL for the present observations and compared it with the results of section 4.2.2. The method is as follows. First, DGL ($\lambda I_{\rm DGL}$) is subtracted from the spectrum of the night sky ($\lambda I_{\rm NS}$). Next, we subtracted the DGL-subtracted spectrum ($\lambda I_{\rm NS} - \lambda I_{\rm DGL}$) and the template of the ZL spectrum $\lambda M_{\rm ZL}$ multiplied by a constant value b and defined that spectrum as $\lambda I_{\rm Atm}$. Finally, we measured the ZL brightness at 400 nm where the correlation coefficient between $\lambda I_{\rm Atm}$ and $b\lambda M_{\rm ZL}$ equals 0 with varying the constant value b.

We show an example of the correlation coefficient for each ZL brightness $b\lambda M_{\rm ZL}$ in figure B.1 and the result of this method in table B.1 (total figure of this analysis shows figure G.7 in appendix G). This figure shows that the difference between this method and the present observation is about a factor of 3. This is because the correlation coefficient between atmospheric light and ZL spectra, which affected the present observation, is 0.6, which is different from the environment observed by Bernstein et al. (2002). For this reason, this method was not employed in this analysis.

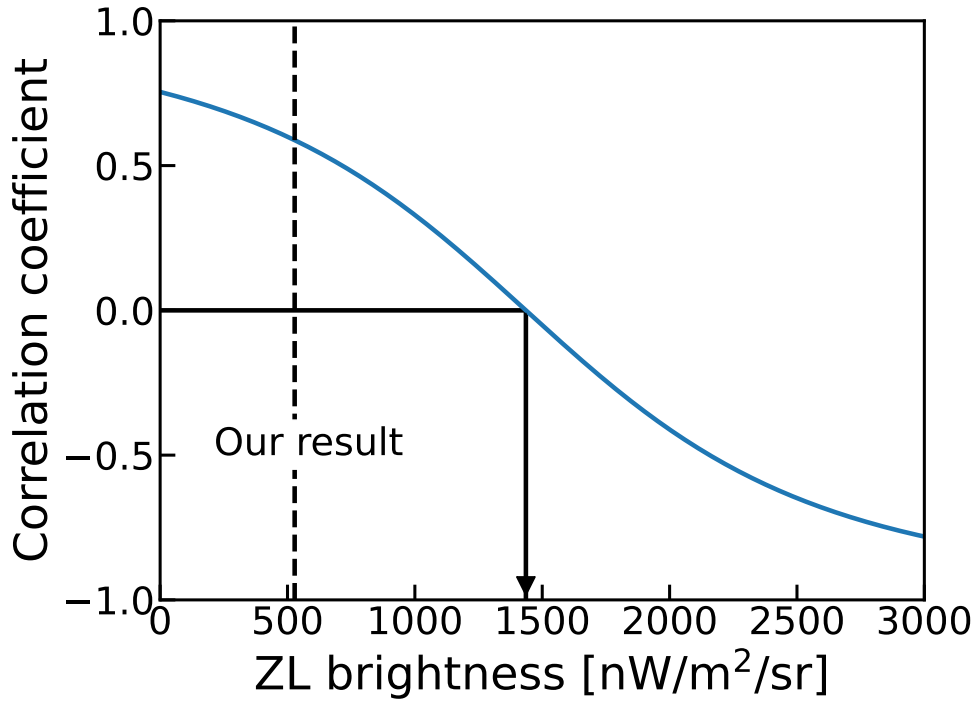

Figure B.1: The ZL brightness of Bernstein et al. (2002) method. The blue line shows the correlation coefficient at each ZL brightness at 400 nm ($b\lambda M_{\mathrm{ZL}}$). The solid means the result of ZL brightness at correlate coefficient = 0. The dashed line means our result (figure 4.9)

Table B.1: ZL brightness of Bernstein et al. (2002).

Field	ZL brightness of this method nW m^{-2} nm^{-1}	this method / our redsult
WISE-J0301	2020.7	4.58
Elon66Step17	1474.9	3.73
Elon66Step28	1268.6	3.60
Elon66Step29	1249.7	3.10
Elon66Step30	1230.6	2.78
Elon82Step6	1435.8	2.72
Elon82Step7	1501.2	2.47

Appendix C

Other creation methods of airglow spectral template

In this study, the difference between Elon66Step28, 29, and 30 from WISE-J0301 was used as the template for airglow. However, according to Figure4.1, the modeled ZL brightness is 10% identical between Elon82Step6 and 7 and Elon66Step17. Therefore, the spectral shape was compared with the airglow spectral template used in this study by taking the difference between the following three patterns; Elon82Step7 minus Elon82Step6, Elon82Step6 minus Elon66Step17, and Elon82Step7 minus Elon66Step17. The spectral shape was compared with the airglow spectral template used in this study. As shown in figure C.1, all of these patterns cannot be used because of the badness of their signal-to-noise ratios (S/N).

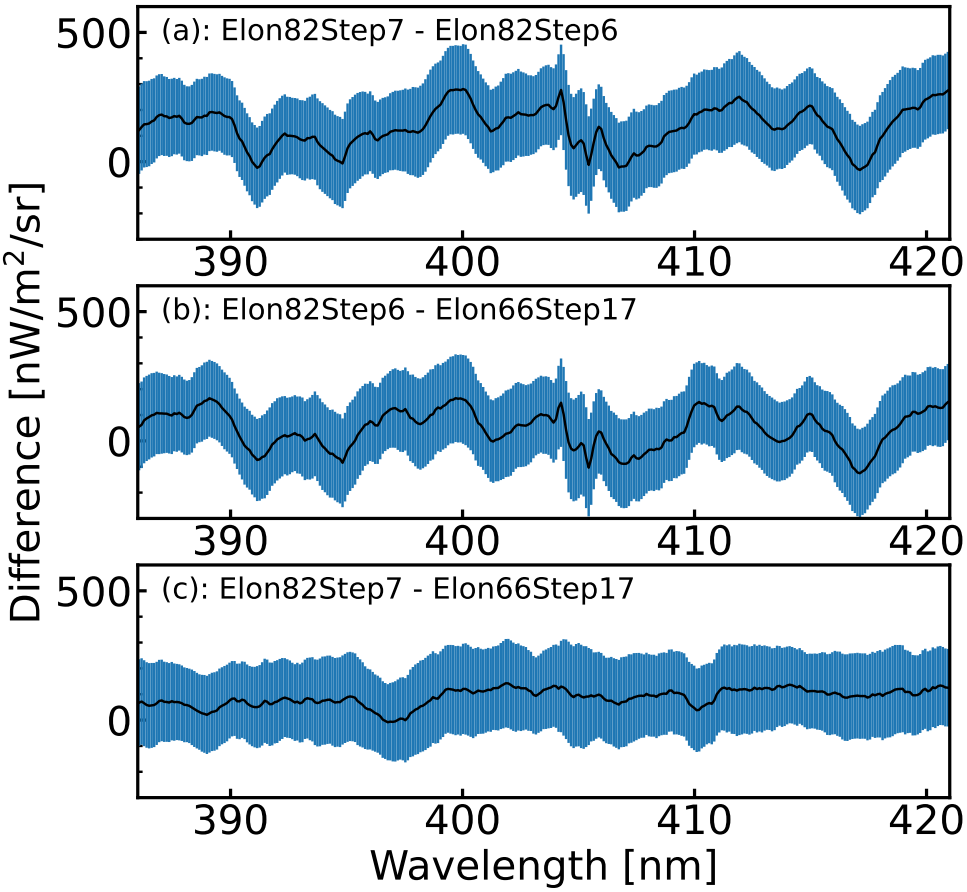

Figure C.1: Other airglow spectral templates. (a) shows Elon82Step7 minus Elon82Step6, (a) shows Elon82Step6 minus Elon66Step17, (c) shows Elon82Step7 minus Elon66Step17.

Appendix D

Kelsall model

In this thesis, we adopted the Kelsall model (Kelsall et al., 1998) as a typical model of ZL brightness. The Kelsall model parameterizes the physical properties of IPD particles based on DIRBE observations.

The ZL brightness $I_{ZL,\lambda}(p,t)$ observed at wavelength λ for observed direction p at the time t is calculated by the integral along the line of sight of scattered and thermal emission contribution and summed over each density component c:

$$I_{ZL,\lambda}(p,t) = \sum_c \int n_c(X,Y,Z)[A_{c,\lambda}F_\lambda^\odot \Phi_\lambda(\Theta) + (1-A_{c,\lambda})E_{c,\lambda}B_\lambda(T)K_\lambda(T)]ds, \tag{D.1}$$

where $n_c(X,Y,Z)$ is the three-dimensional density at the position (X,Y,Z) for each of the components, $A_{c,\lambda}$ is the albedo for component c at wavelength λ, $F_\lambda^\odot$ is the solar flux, $\Phi_\lambda(\Theta)$ is the phase function at scattering angle Θ, $E_{c,\lambda}$ is an emissivity modification factor that measures deviations from the blackbody thermal radiance function $B_\lambda(T)$, and $K_\lambda(T)$ is the DIRBE color-correction factor appropriate for $B_\lambda(T)$. The dust grain temperature T is assumed to vary with distance from the Sun as $T(R) = T_0 R^{-\delta}$. The derived model value of $\delta = 0.467$ is very close to the theoretical value of 0.5 for large gray grains in radiative equilibrium.

The Kelsall model assumes that the density components c consist of three components: smooth cloud, dust bands, and circumsolar ring. The smooth cloud is the origin of Jupiter's family comets (JFCs), short-period comets from the Edgeworth-Kuiper belt. The dust bands and circumsolar ring are the origin of asteroids and the ring-shaped components in the orbit of Earth.

In Figure D.1, we show the density distribution of each component c.

The center of the smooth cloud was allowed to be offset from the Sun by (X_0, Y_0, Z_0), so that the cloud coordinates were translated as follows:

$$\begin{aligned} X' &= X - X_0, \\ Y' &= Y - Y_0, \\ Z' &= Z - Z_0, \\ R_c &= \sqrt{X'^2 + Y'^2 + Z'^2}. \end{aligned}$$

The symmetry plane of the smooth cloud was also allowed to be tilted with respect to the ecliptic plane, so that the vertical structure is dictated by the height above the tilted midplane;

$$Z_c = X' \sin\Omega \sin i - Y' \cos\Omega \sin i + Z' \cos i, \tag{D.2}$$

where i and Ω are the inclination and ascending node of the midplane, respectively. The density of the smooth cloud was presumed to be of a form that is separable into radial and vertical terms:

$$n_c(X', Y', Z_c) = n_0 R_c^{-\alpha} f(|Z_c/R_c|), \tag{D.3}$$

where n_0 is the IPD density at $R = 1$ AU, α is the radial power-law index motivated by the radial distribution under the Poynting-Robertson effect, $f(|Z_c/R_c|)$ is the vertical distribution and written in a form representing a widened, modified fan model:

$$f(|Z_c/R_c|) = e^{-\beta g^\gamma} \tag{D.4}$$

where

$$g = \begin{cases} (Z_c/R_c)^2/2\mu & (|Z_c/R_c| < \mu) \\ |Z_c/R_c| - \mu/2 & (|Z_c/R_c| \geq \mu) \end{cases} \tag{D.5}$$

and β, γ and μ are free parameters.

The density of the dust band consists of three components; Themis and Koronis families ($\pm 1°.4$)、the Eos asteroid family ($\pm 10°$)、Maria/Io family ($\pm 15°$). All band pairs were centered on the Sun, but were allowed to be inclined with respect to the ecliptic plane. A transformation with equation D.2 was used to define the vertical distance from the midplane of band pair i, Z_{Bi}.

$$n_{B,i} = \frac{3n_{3Bi}}{R} \exp\left[-\left(\frac{|Z_{B,i}/R_c|}{\delta_{\zeta_{B,i}}}\right)^6\right]\left[v_{B,i} + \left(\frac{|Z_{B,i}/R_c}{\delta_{\zeta_{B,i}}}\right)^{p_{B,i}}\right] \times\left\{1 - \exp\left[-\left(\frac{R}{\delta_{R_{B,i}}}\right)^{20}\right]\right\}, \tag{D.6}$$

where n_{3Bi} is the density at 3 AU of band i, $\delta_{\zeta_{B,i}}$, $v_{B,i}$, and $p_{B,i}$ are adjustable shape parameters, and $\delta_{R_{B,i}}$ determines the distance to which band i migrates in toward the Sun.

The circumsolar ring is the dust component bound by the gravity of the Earth to resonant orbits near 1 AU. The circumsolar ring consists of the ring component and trailing blob. This component is allowed to be inclined with respect to the ecliptic plane; the vertical distance above the ring midplane is denoted by Z_R and is computed using equation D.2. The three-dimensional ring dust density distribution is modeled as

$$n_R(X,Y,Z) = n_{SR} \exp\left[-\frac{(R - R_{SR})^2}{2\sigma_{rSR}^2} - \frac{|Z_R|}{\sigma_{rSR}}\right] + n_{TB} \exp\left[-\frac{(R - R_{TB})^2}{2\sigma_{rTB}^2} - \frac{|Z_R|}{\sigma_{zTB}} - \frac{(\theta - \theta_{TB})^2}{2\sigma_{\theta TB}}\right], \tag{D.7}$$

where the subscript SR stands for the circumsolar ring and TB stands for the trailing blob. The σ values are free parameters for scale lengths in the R,Z_R, and θ coordinates. Also free are the radial locations of the peak density of the ring R_{SR} and blob R_{TB} and the peak densities n_{SR} and n_{TB}.

See Kelsall et al. (1998) for more details and the value of the observed parameters.

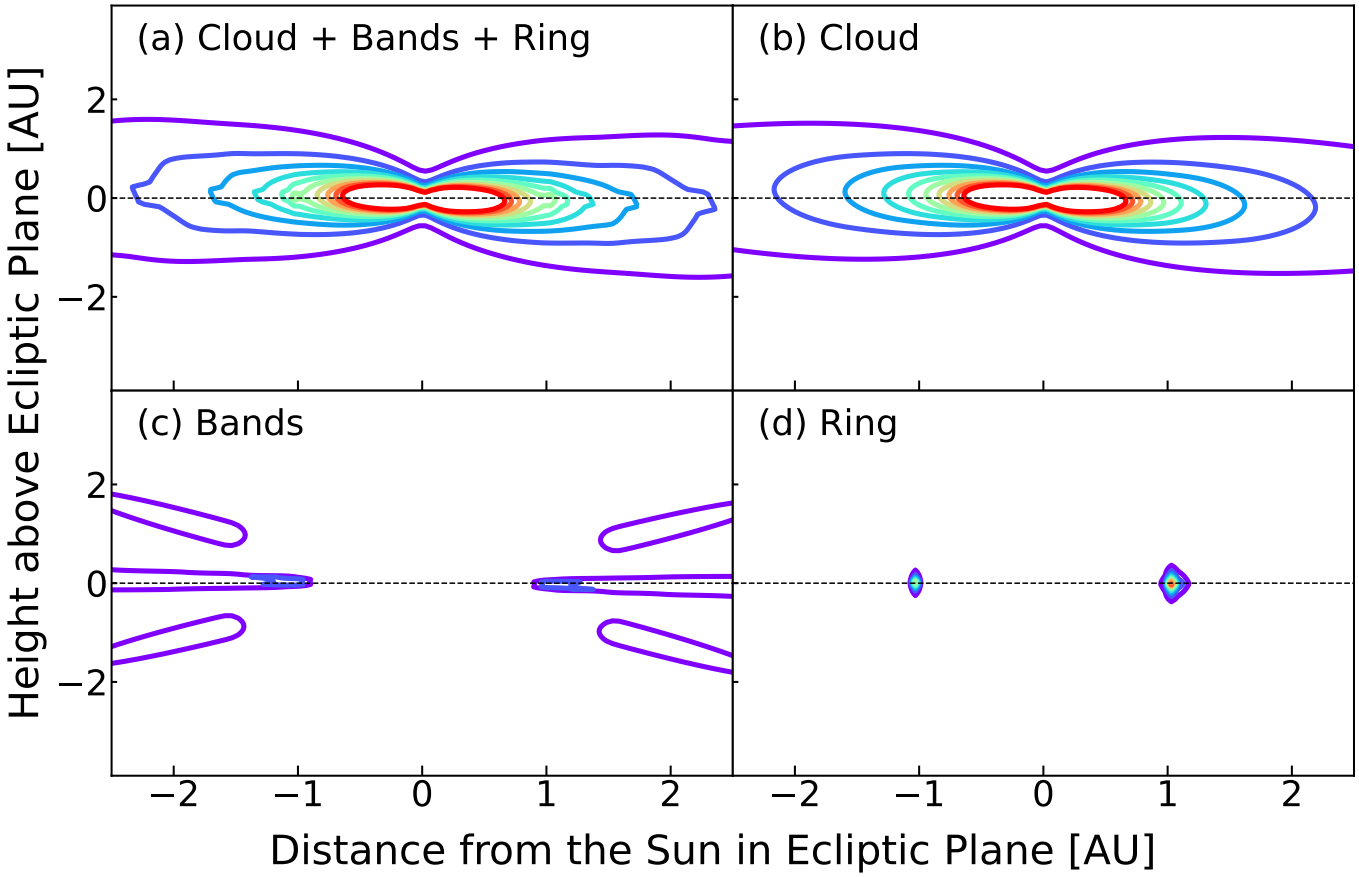

Figure D.1: The three-dimensional density distribution of IPD particles calculated by the Kelsall model simulated by *Zodipy*. These figures show a cross-sectional slice perpendicular to the ecliptic plane. (a) : Summed up of all components. (b) : Smooth cloud. (c) : Dust bands. (d) : Circumsolar ring.

Appendix E

The validity of airglow spectral template

In this section, we compare our airglow spectral template (figure 4.2) and the previous research (figure E.2 and E.1, Krassovsky et al. , 1962 and Broadfoot and Kendall , 1968) to check that our template is correct.

Comparing figure E.1 and figure 4.2, we see that we agree on the continuum having a peak around 450 nm. In addition, comparing figure E.2 and figure 4.2, the emission line profiles around Ca II $\lambda\lambda$ 393.3, 396.8 nm and the strong emission line (Hg) at 430 nm are consistent. The airglow spectral template adopted in this study has the characteristics of both Krassovsky et al. (1962) and Broadfoot and Kendall (1968).

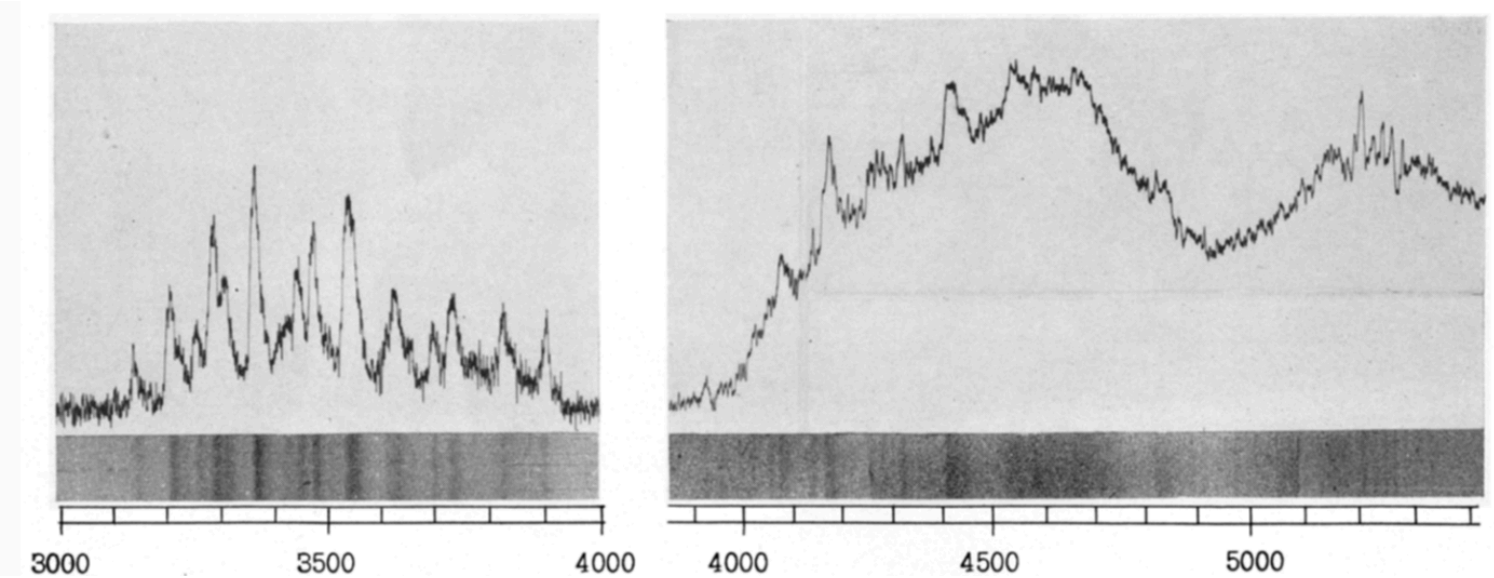

Figure E.1: The airglow spectrum from Krassovsky et al. (1962) as unit of Å.

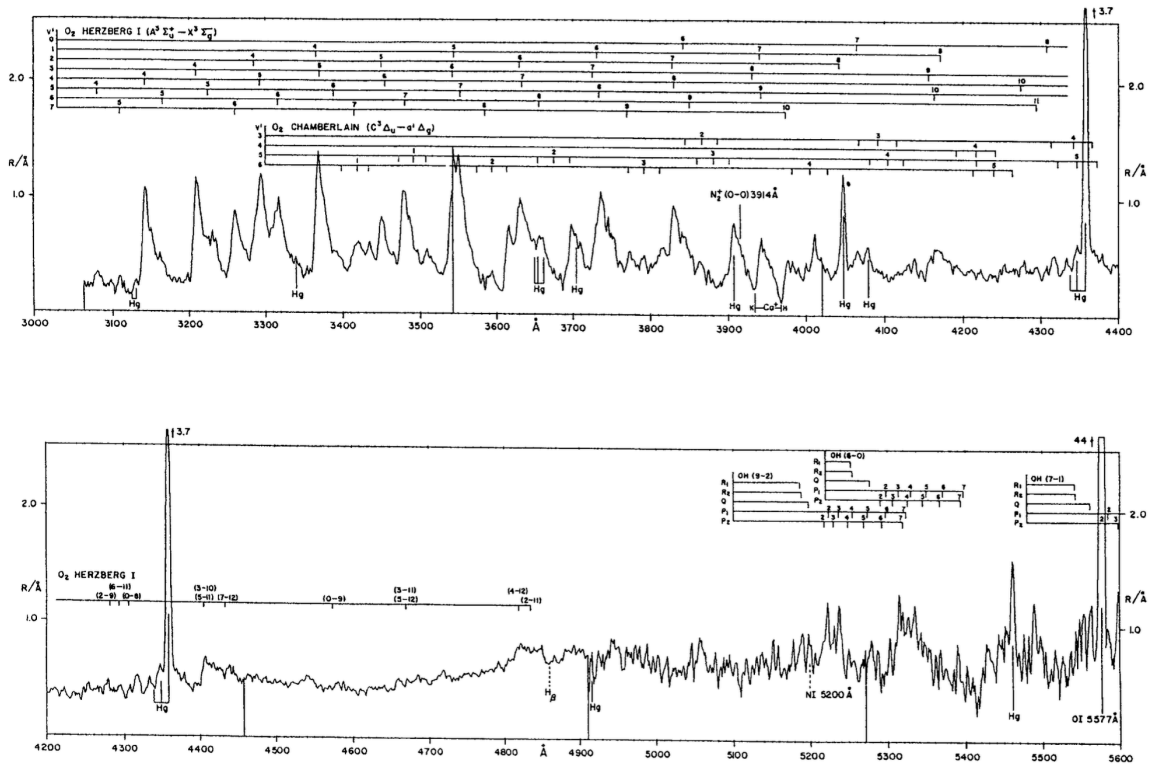

Figure E.2: The airglow spectrum from Broadfoot and Kendall (1968). The horizontal axis shows the wavelength as the unit of Å, the vertical axis shows the intensity. The top image shows the wavelength range from 300 nm to 400 nm and the bottom shows from 420 nm to 560 nm.

Appendix F

Fitting argolitm

We used the non-linear least squares as a method for fitting the measured data with a non-linear function. This method cannot estimate the best-fitted parameter analytically as opposed to linear least squares. Therefore, there is the iterative method as a method of estimation of the best-fitted parameters. The iterative method follows the following steps;

- Step0 : Input the matrix of initial parameters,
- Step1 : Calculate the reduced chi-square,
- Step2 : Update the matrix of parameters followed by the recurrence relation,
- Step3 : Return to Step1 if the calculated reduced-chi square is large.

In this study, we adopt the Levenberg-Marquardt algorithm in the iterative method. This algorithm is the method that combines the Gauss-Newton algorithm and gradient descent. In this chapter, we describe the Levenberg-Marquardt algorithm after the Gauss-Newton algorithm and gradient descent. In addition, we define that $(\boldsymbol{x}, \boldsymbol{y})$ is the m-dataset, $f(\boldsymbol{x}, \boldsymbol{\beta})$ is the fitting function with the parameter matrix $\boldsymbol{\beta}$, and the residual is $\boldsymbol{r} = \boldsymbol{y} - f(\boldsymbol{x}, \boldsymbol{\beta})$ in this chapter.

F.1 Gauss-Newton algoritm

Gauss-Newton algorithm is the one method to solve the non-linear least squares. The algorithm finds the parameter for which the sum of squares

of the residuals (S, written in equation F.1) is the smallest (theoretically 0) with equation F.2.

$$S(\boldsymbol{\beta}) = \sum_{i=1}^{m} \boldsymbol{r}^2(\boldsymbol{\beta}), \tag{F.1}$$

$$\boldsymbol{\beta}_{k+1} = \boldsymbol{\beta}_k + (\boldsymbol{J}^T\boldsymbol{J})^{-1}\boldsymbol{J}^T\boldsymbol{r}, \tag{F.2}$$

where $\boldsymbol{J}$ is the jacobian of $\boldsymbol{r}$. This method is fast in computation but has the disadvantage of failing to converge if the initial parameters $\boldsymbol{\beta}_{k=0}$ are far from the true parameters.

F.2 Gradient descent

The gradient descent is the method to find the parameter matrix when the residual $\boldsymbol{r}(\boldsymbol{\beta})$ is the smallest using the gradient of the $\boldsymbol{r}$. The recurrence relation is equation F.3;

$$\boldsymbol{\beta}_{k+1} = \boldsymbol{\beta}_k - \alpha\nabla\boldsymbol{r}, \tag{F.3}$$

where α means the small-positive value. This algorithm is simple, but it has the possibility of diverging in the middle of the calculation.

F.3 Levenberg-Marquardt algorithm

Levenberg-Marquardt algorithm behaves like the Gauss-Newton algorithm when the parameter matrix is near the true, and the gradient descent when the parameter matrix is bad. The recurrence relation is equation F.4;

$$\boldsymbol{\beta}_{k+1} = \boldsymbol{\beta}_k + (\boldsymbol{J}^T\boldsymbol{J} + \lambda_k\boldsymbol{I})^{-1}\boldsymbol{J}^T\boldsymbol{r}, \tag{F.4}$$

where λ_k is the small-positive value, $\boldsymbol{I}$ is the identity matrix.

See Björck (1996) (Gauss-Newton algorithm), Boyd&Vandenberghe (2004) (Gradient descent), Levenberg (1944) and Marquardt (1963) (Levenberg-Marquardt algorithm) for the proof and details.

Appendix G

Extra figure

In this chapter, we show figures that we could not include in the text. Figure G.1 is the spectrum of the night sky observed at night. Figure G.2 shows the number of stars that enter the slit in each observation. Figure G.3 shows the number of stars entering the slit for each observation. Figure G.5 shows the ZL brightness for different wavelength ranges during the fitting. Figure G.6 is the ZL brightness (200 steps) when the airglow spectral template is varied using a Monte Carlo simulation. Figure G.7 is the ZL brightness obtained by the method of Bernstein et al. (2002).

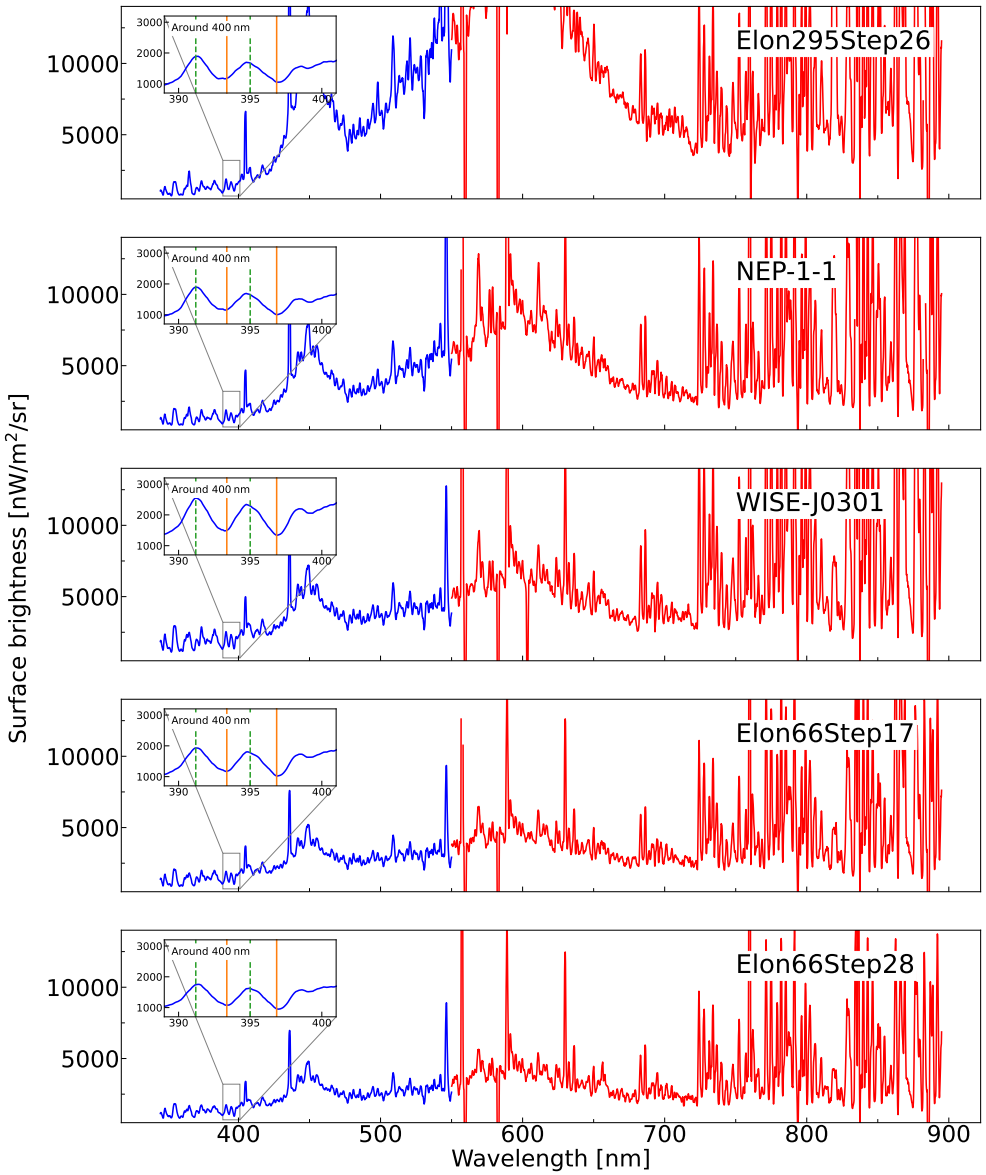

Figure G.1: Observed night-sky spectra. The blue shows the blue channel and red shows the red channel of DBSP. The zoomed figure shows around 400 nm, which exist the deepest Fraunhofer lines CaIIλ λ393.3 396.8 nm.

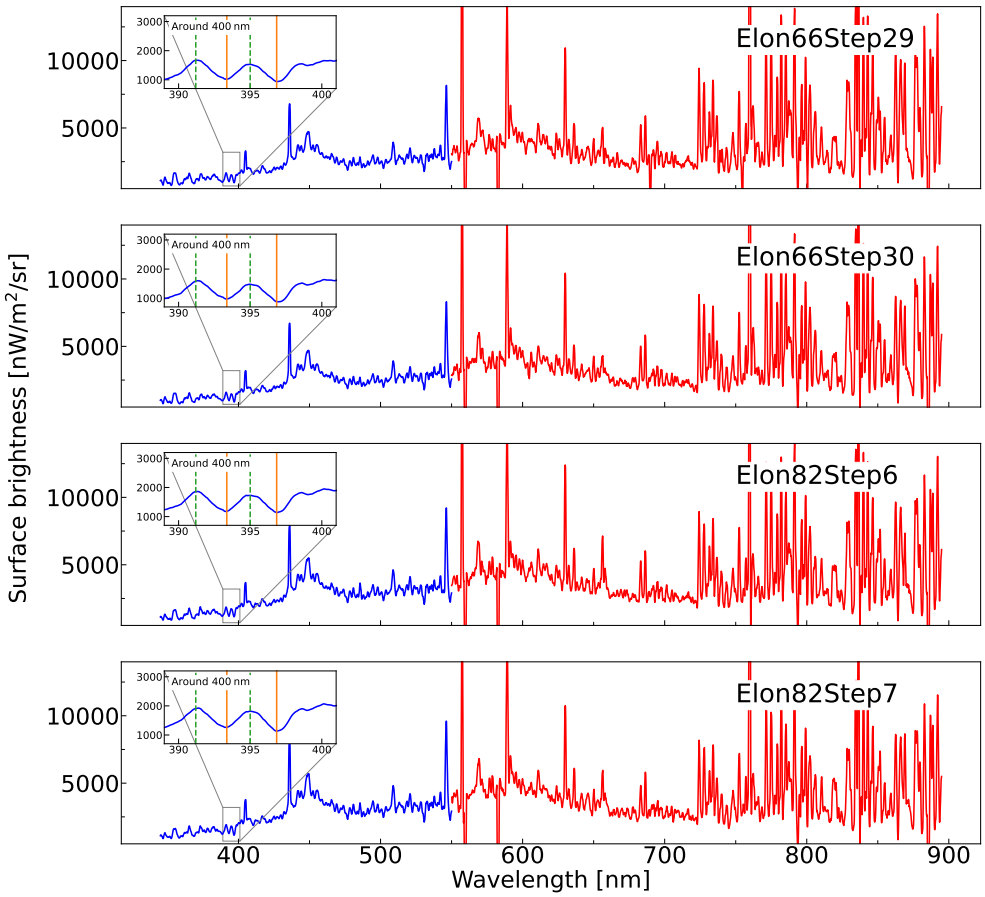

Figure G.1: Cotinue.

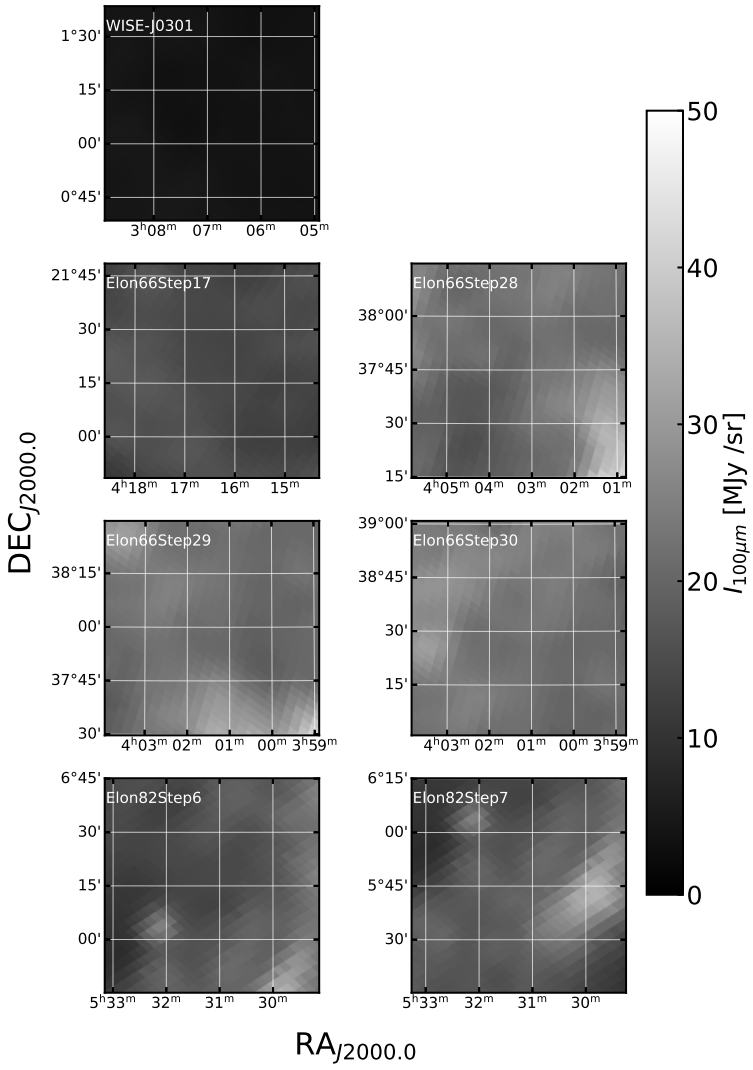

Figure G.2: All images of 100 μm intensity by Schlegel et al. (1998).

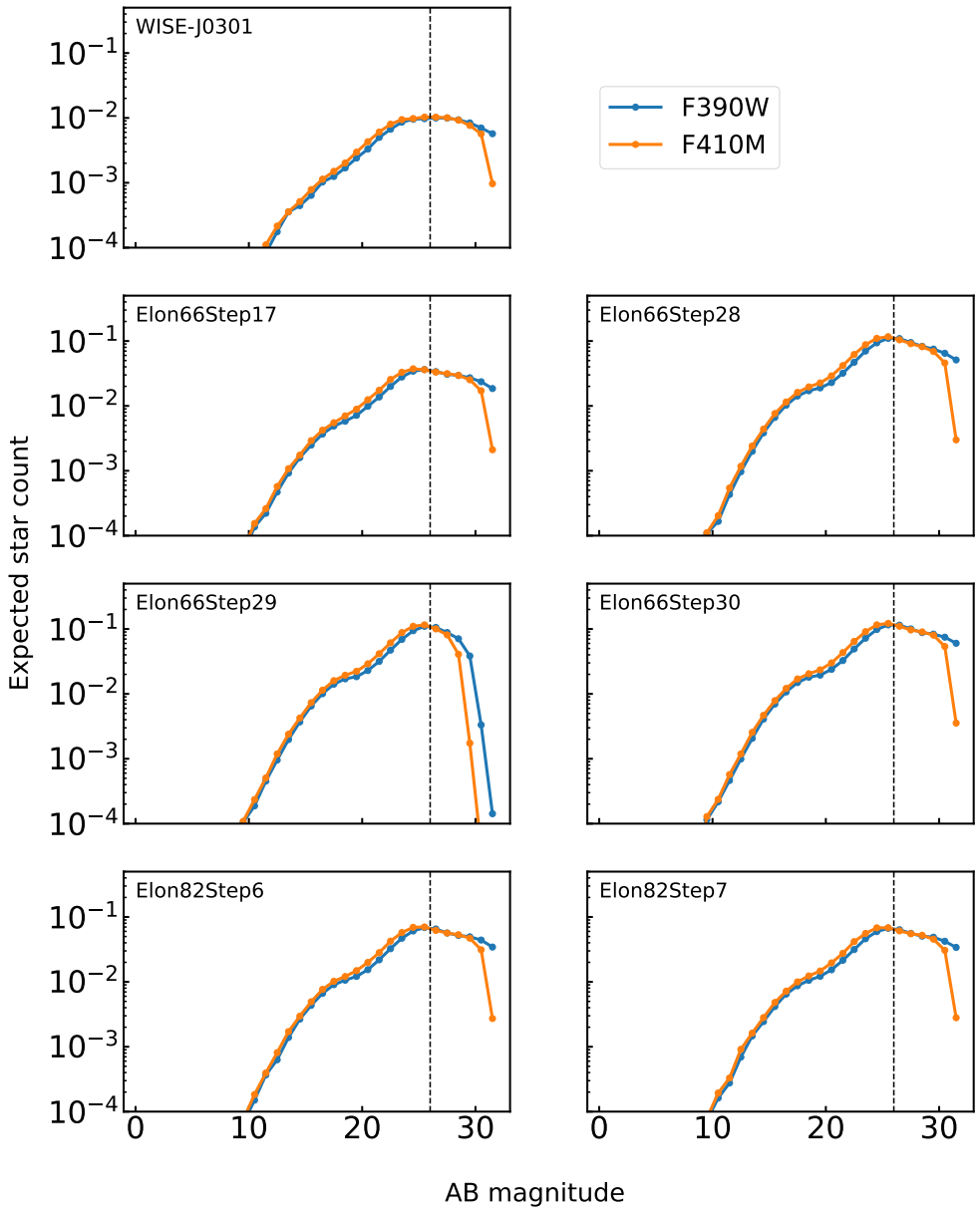

Figure G.3: All images of the expected star count within the observed slit area. The blue line of each image shows the result estimated by F390W and the orange shows F410M.

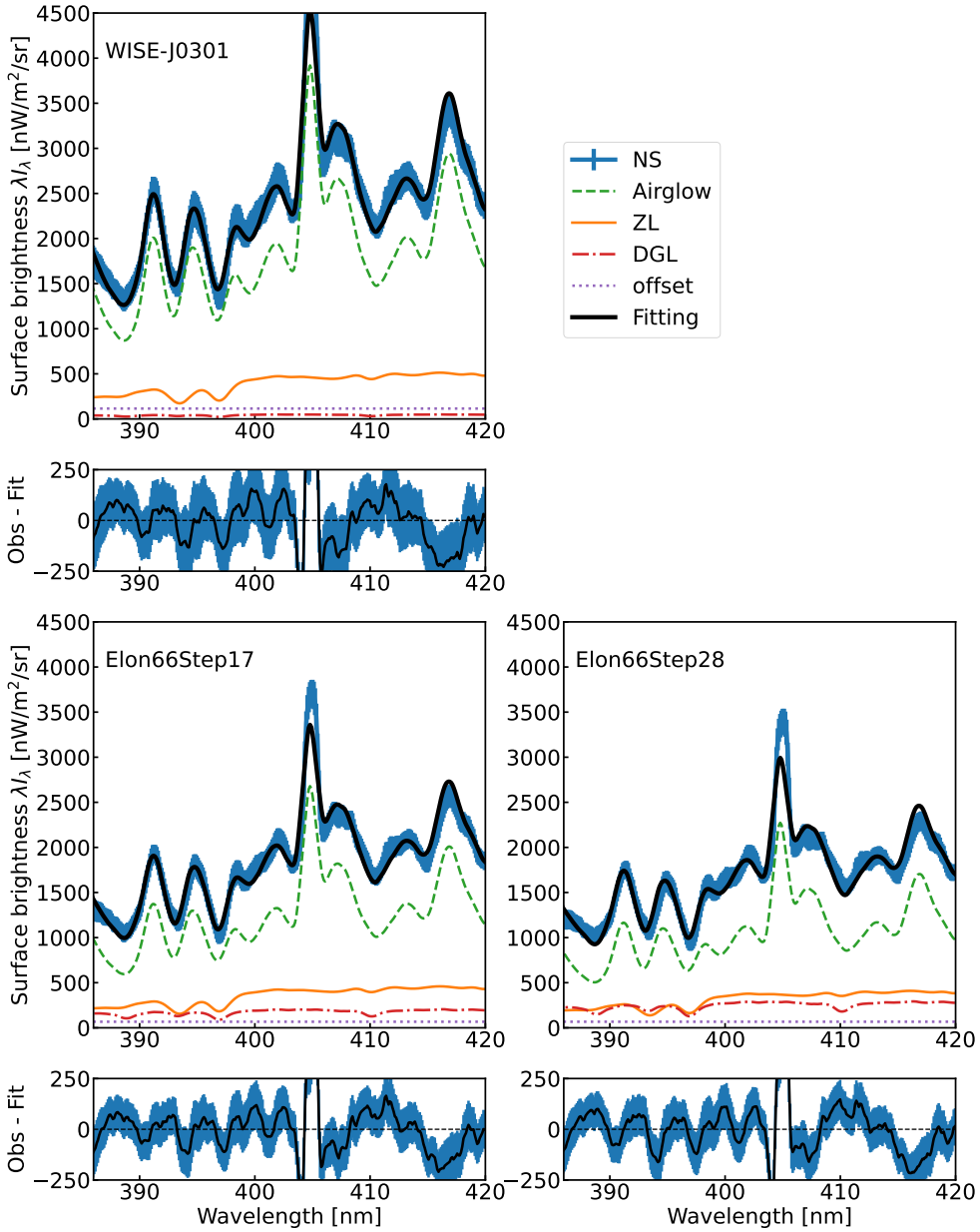

Figure G.4: All image of result of fitting by equation 4.1. At the top of each image, the blue line shows observed night-sky spectra, green shows airglow, orange shows ZL, red shows DGL, purple shows offset light, and black is a fitting result. The bottom of each image shows the observed data (the blue line of the top image) minus fitting (the black line).

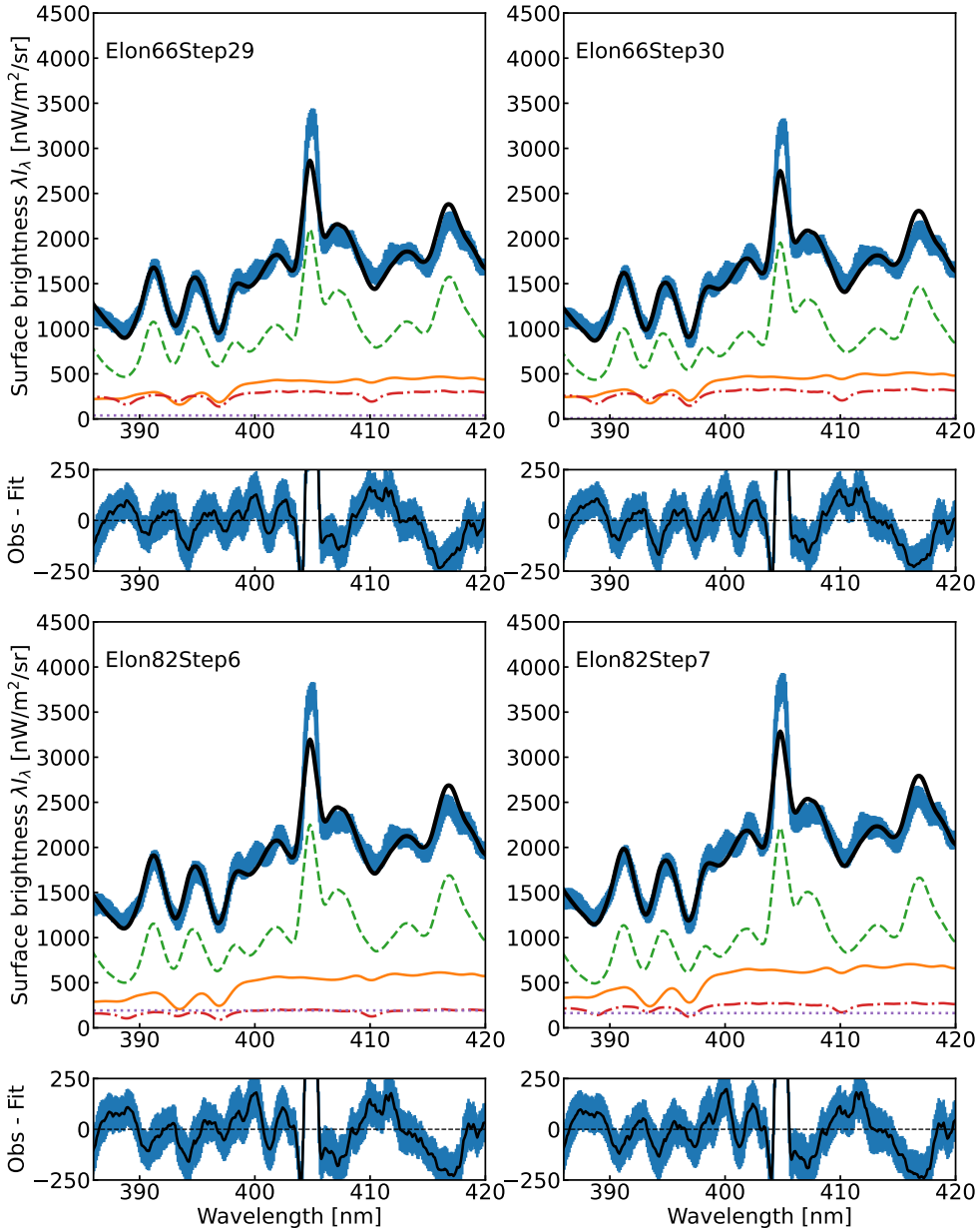

Figure G.4: Continue.

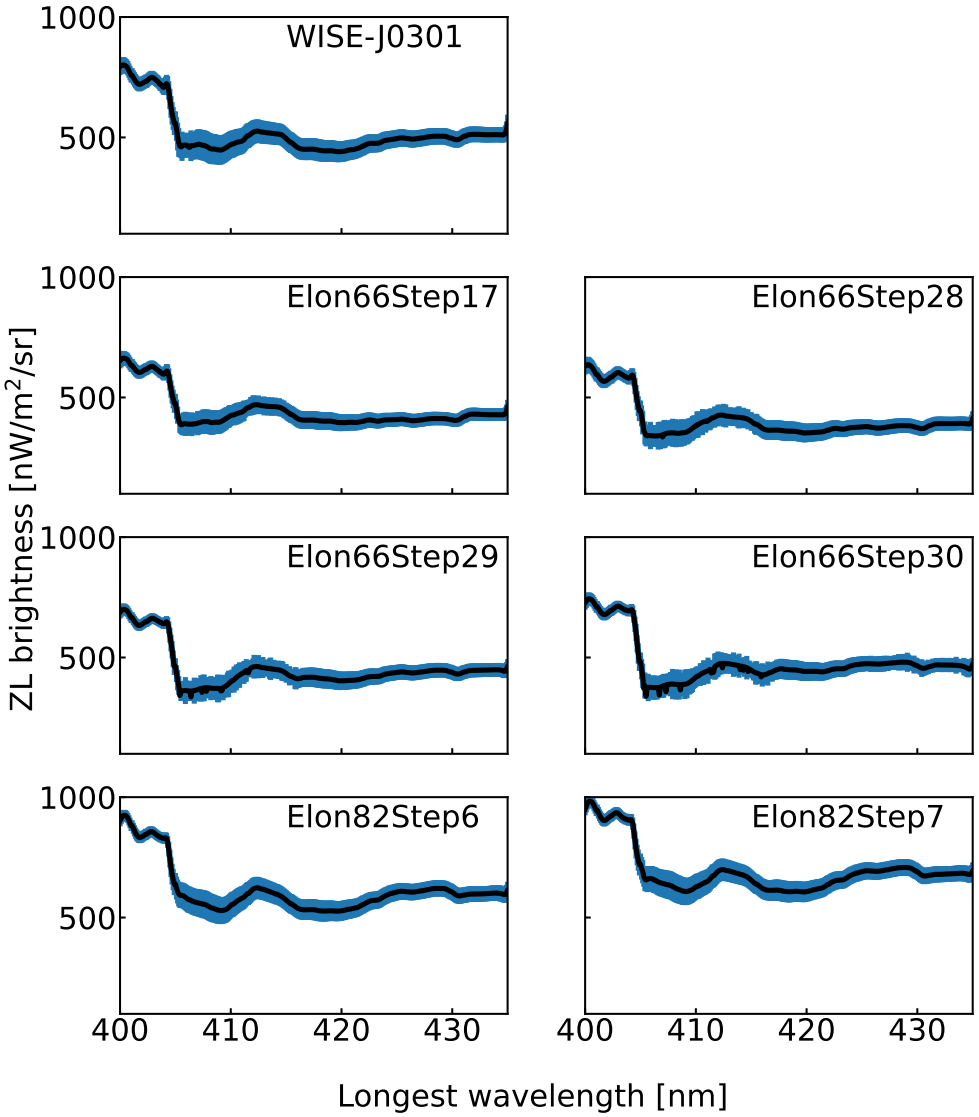

Figure G.5: Variation of the ZL brightness at 400 nm for different fitting wavelengths. The horizontal axis is the end of the fitting wavelength. The colors of the figure are the same as in figure 4.10.

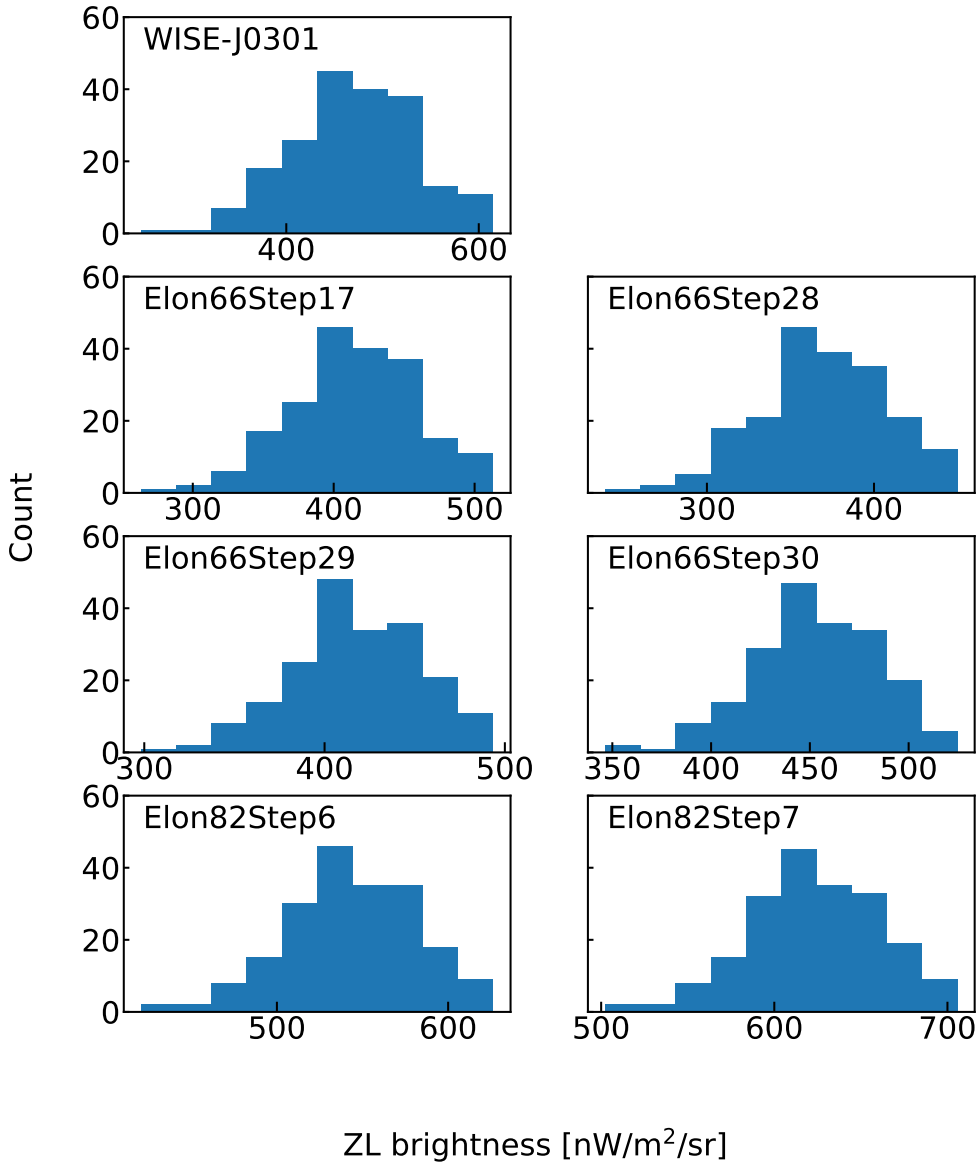

Figure G.6: The resultants of the Monte-Carlo simulation to indicate the uncertainty of the ZL brightness. Histograms is the same as figure 4.11.

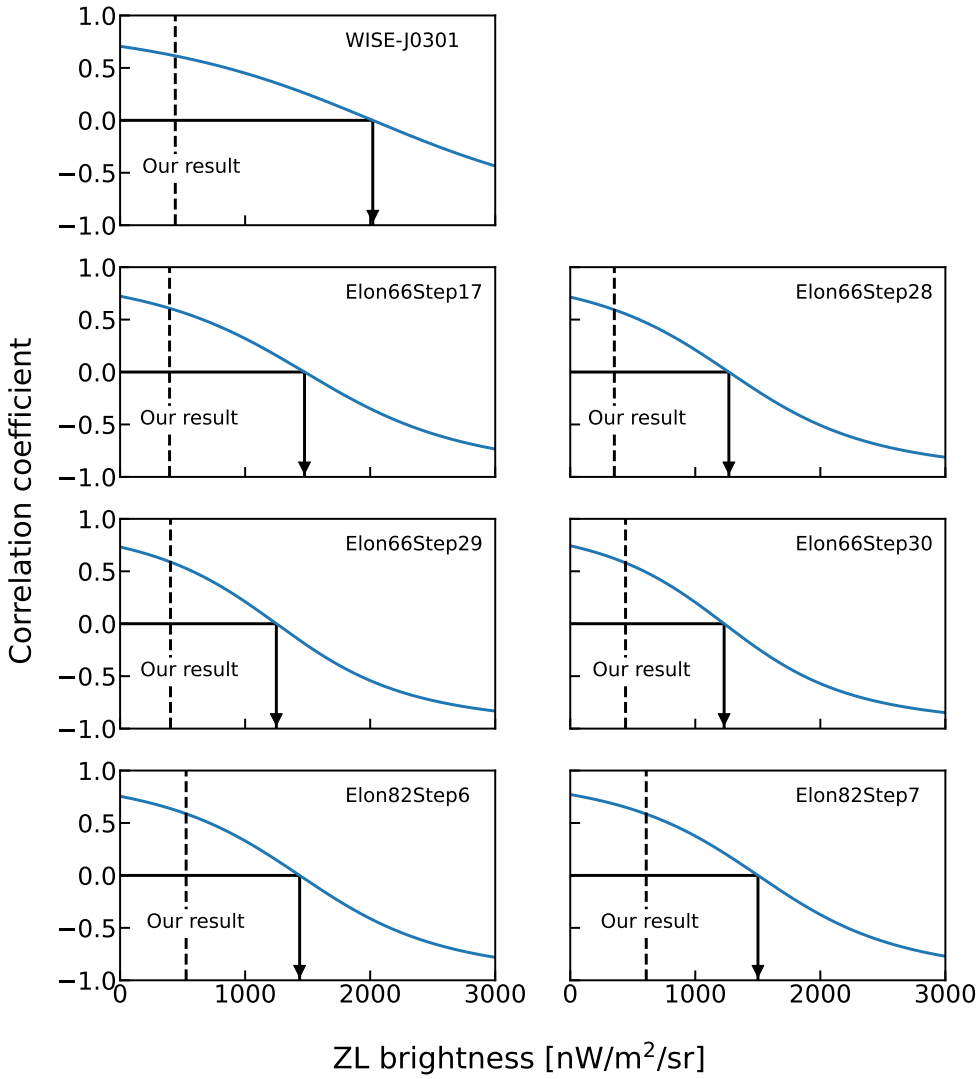

Figure G.7: The result of ZL brightness estimated by the method of Bernstein et al. (2002). The solid line means our result as shown in section4.2.2.

Reference

Accetta, K, A., et al. 2022, "The Seventeenth Data Release of the Sloan Digital Sky Surveys: Complete Release of MaNGA, MaStar, and APOGEE-2 Data", ApJS, 259, 35

Berk, A., Conforti, P., Kennett, R., Perkins, T., Hawes, F., & van den Bosch, J., 2014, "MODTRAN6: a major upgrade of the MODTRAN radiative transfer code", Proc. SPIE 9088,90880H

Berk, A., Conforti, P., Hawes, F., 2015, "An accelerated line-by-line option for MODTRAN combining on-the-fly generation of line center absorption with 0.1 cm-1 bins and pre-computed line tails", Proc. SPIE 9471, 947217

Bernstein, R, A., Freedman, W, L.& Madore, B, F., 2002, "THE FIRST DETECTIONS OF THE EXTRAGALACTIC BACKGROUND LIGHT AT 3000, 5500, AND 8000 Å . II. MEASUREMENT OF FOREGROUND ZODIACAL LIGHT", ApJ, 517, 85

Björck, A., 1996, "Numerical Methods for Least Squares Problems", SIAM (Philadelphia, the United States of America)

Boyd, S., & Vandenberghe, L., 2004, "Convex Optimization", Cambridge University Press (New York), 457 - 520

Brian, H M, 2007, "A SURVEY OF RADIAL VELOCITIES in the ZODIACAL DUST CLOUD", PhD thesis, Imperial College

Broadfoot, A L & Kensall, K. R, 1968, "The Airglow Spectrum, 3100-10000Å", Journal of Geophysical Research (United States of America), 73, 426

Calamida, A., et al. 2019,"Photometry and Spectroscopy of Faint Candidate Spectrophotometric Standard DA White Dwarfs", ApJ, 872, 199

Carleton, T., et al. 2022, "SKYSURF: Constraints on Zodiacal Light and Extragalactic Background Light through Panchromatic HST All-sky Surface-brightness Measurements: II. First Limits on Diffuse Light at 1.25, 1.4, and 1.6μm", Astronomical Journal, 164,170

Driver, S P. et al., 2016, "MEASUREMENTS OF EXTRAGALACTIC BACKGROUND LIGHT FROM THE FAR UV TO THE FAR IR FROM DEEP GROUND- AND SPACE-BASED GALAXY COUNTS", ApJ, 827, 108

Dwek, E. & Arendt, R. G, 1998, "A Tentative Detection of the Cosmic Infrared Background at 3.5 μm from COBE/DIRBE Observations", ApJ, 508,1,L9-L12

Fazio, G. G., et al. 2004, "The Infrared Array Camera (IRAC) for the Spitzer Space Telescope", ApJS 154,10-17

Girardi, L., Groenewegen, M. A. T., Hatziminaoglou, E. & da Costa, L., 2005, "SStar counts in the Galaxy. Simulating from very deep to very shallow photometric surveys with the TRILEGAL code", A&A, 436, 895-915

Girardi, L. & Marigo, P., 2007, "Towards Simulating the Photometry, Chemistry, Mass Loss and Pulsational Properties of AGB Star Populations in Resolved Galaxies", ASP Conference Series, 378, 20

Girardi, Léo., et al., 2012, "TRILEGAL, a TRIdimensional modeL of thE GALaxy: Status and Future", Astrophysics and Space Science Proceedings (Berlin: Springer), 26, 165

Groenewegen, M. A. T., et al. 2002, "ESO Imaging Survey. The stellar catalogue in the Chandra deep field south", A&A , 392, 741-755

Hayes, D. S. & Latham, D. W. 1975, "A REDISCUSSION OF THE ATMOSPHERIC EXTINCTION AND THE ABSOLUTE SPECTRAL-ENERGY DISTRIBUTION OF VEGA", ApJ, 197, 593-601

Kashlinsky, A., Arendt, R. G., Atrio-Barandela, F., Cappelluti, N., Ferrara, A., & Hasinger, G., 2018, "Looking at cosmic near-infrared background radiation anisotropies", Reviews of Modern Physics, 90, 025006

Kawara, K., Matsuoka, Y., Sano, K., Brandt, T. D., Sameshima, H., Tsumura, K., Oyabu, S., & Ienaka, N., 2017, "Ultraviolet to optical diffuse sky emission as seen by the Hubble Space Telescope Faint Object Spectrograph", PASJ, 69, 31

Kelsall, T., et al. 1998, "THE COBE DIFFUSE INFRARED BACKGROUND EXPERIMENT SEARCH FOR THE COSMIC INFRARED BACKGROUND. II. MODEL OF THE INTERPLANETARY DUST CLOUD", ApJ, 508, 44

Krassovsky, V. I., Shefov, N. N., & Yarin, V. I., 1962, "Atlas of the airglow spectrum 3000-12400 Å", Planetary and Space Science, 9, 883

Lauer, Tod R. et al., 2022, "Anomalous Flux in the Cosmic Optical Background Detected with New Horizons Observations", ApJL, 927, L8

Leinert, Ch., et al. 1998, "The 1997 reference of diffuse night sky brightness", A&AS, 127, 1-99

Levenberg, K., 1944, "A method for the solution of certain non-linear problems in least squares", Quarterly of Applied Mathematics, 2, 164 - 168

Liou, J. C., Dermott, S. F., & Xu, Y. L., 1995, "The contribution of cometary dust to the zodiacal cloud", P&SS, 43, 717-722

Marquardt, D., 1963, "An Algorithm for Least-Squares Estimation of Nonlinear Parameters", SIAM Journal on Applied Mathematics, 11, 431 - 441

Matsuura, S., et al. 2017, "New Spectral Evidence of an Unaccounted Component of the Near-infrared Extragalactic Background Light from the CIBER", ApJ, 839

Matsumoto, T., Kim, M. G., Pyo, J., & Tsumura, K., 2015, "REANALYSIS OF THE NEAR-INFRARED EXTRAGALACTIC BACKGROUND LIGHT BASED ON THE IRTS OBSERVATIONS", ApJ, 807, 57

Mattila. K., Väisänen, P., Lehtinen. K., von Appen-Schnur, G.& Leinert. Ch., 2017, "Extragalactic background light: a measurement at 400 nm using dark cloud shadow - II. Spectroscopic separation of the dark cloud's light, and results", MNRAS, 470, 2152-2169

Miville-Deschênes, M. -A., & Lagache, G., 2005, "IRIS: A NEW GENERATION OF IRAS MAPS", ApJ, 157, 302

Narayan, G., et al. 2019, "Subpercent Photometry: Faint DA White Dwarf Spectrophotometric Standards for Astrophysical Observatories", ApJ Supplement, 241, 41

Nesvorný, D., Bottke, W, F., Levison, H, F., Dones, L., 2003, "RECENT ORIGIN OF THE SOLAR SYSTEM DUST BANDS", ApJ, 591, 486

Nesvorný, D., Jenniskens, P., Levinson, H, F., Bottke, W, F., Vonkrouhlický, D., & Gounelle, M., 2010, "COMETARY ORIGIN OF THE ZODIACAL CLOUD AND CARBONACEOUS MICROMETEORITES. IMPLICATIONS FOR HOT DEBRIS DISKS", ApJ, 816-836

Oke. J. B., & Gunn, J. E., 1982, "AN EFFICIENT LOW- AND MODERATE-RESOLUTION SPECTROGRAPH FOR THE HALE TELESCOPE", PASP, 94, 586

Onishi, Y., et al. 2018, "MIRIS observation of near-infrared diffuse Galactic light", PASJ, 70, 76

Poppe, A. R., 2016, "An improved model for interplanetary dust fluxes in the outer Solar System", Icarus, 264, 369 - 386

San, M., Herman, D., Erikstad, G. B., Gallowaym, M., and Watts, D., 2022, "COSMOGLOBE: Simulating zodiacal emission with ZodiPy", A&A, 666, A107

Sano, K., Matsuura, S., Yomo, K., & Takahashi , A., 2020, "The Isotropic Interplanetary Dust Cloud and Near-infrared Extragalactic Background Light Observed with COBE/DIRBE", ApJ, 901, 112

Schlegel. D. J., Finkbeiner. D. P.& Davis. M., 1998, "MAPS OF DUST INFRARED EMISSION FOR USE IN ESTIMATION OF REDDENING AND COSMIC MICROWAVE BACKGROUND RADIATION FOREGROUNDS", ApJ, 500, 525-553

Sykes, M. V., & Greenberg, R., 1986, "The formation and origin of the IRAS zodiacal dust bands as a consequence of single collisions between asteroids", Icarus, 65, 51 - 69

Symons, T., Zemcov, M., Cooray, A., Lisse, C., & Poppe, A R., 2023, "A Measurement of the Cosmic Optical Background and Diffuse Galactic Light Scaling from the $R < 50$au New Horizons-LORRI Data", ApJ, 945, 45

Takahashi, A., Ootsubo, T., Matsuhara, H., Sakon, I., Usui, F., & Chihara, H., 2019, "Mid-infrared spectroscopy of zodiacal emission with AKARI/IRC", PASJ, 71, 110

Tsumura, K., Matsumoto, T., Matsuura, S., Sakon, I., & Wada, T., 2013, "Low-Resolution Spectrum of the Extragalactic Background Light with the AKARI InfraRed Camera", PASJ, 65, 121

Vanhollebeke, E., Groenewegen. M. A. T. & Girardi. L., 2009, "Stellar populations in the Galactic bulge Modelling the Galactic bulge with TRILEGAL", A&A,498,95-107

Wright, E. L., 1998, "ANGULAR POWER SPECTRA OF THE COBE DIRBE MAPS", ApJ 496,1-8